J. Fluid Mech. (2025), *vol.* 1016, A46, doi:10.1017/jfm.2025.10424

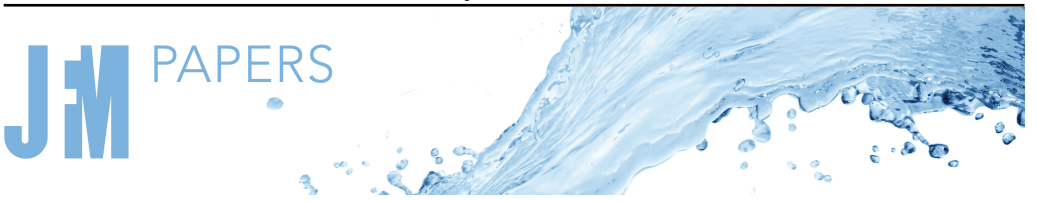

Convection in slender Rayleigh–Bénard cells is a combination of wall and tube components

M.G. Visakh[1] **and Jaywant H. Arakeri**[1,2,3]

[1]Department of Mechanical Engineering, Indian Institute of Science, Bangalore 560012, India

[2]Department of Mechanical Engineering, Indian Institute of Technology Jodhpur, Jodhpur 342027, India

[3]Jawaharlal Nehru Centre for Advanced Scientific Research, Bangalore 560064, India

Corresponding author: M.G. Visakh, visakhmg@iisc.ac.in, visakhmg.iisc@gmail.com

(Received 9 July 2024; revised 2 June 2025; accepted 29 June 2025)

A model for obtaining scaling laws for Rayleigh–Bénard convection (RBC) at high Rayleigh numbers in tall, slender cells (cells with low aspect ratio, $\Gamma = d/H \ll 1$) is presented. Traditional RBC ($\Gamma \gtrsim 1$) is characterised by large-eddy circulation scaling with the height of the cell, a near-isothermal core and almost all the thermal resistance provided at the horizontal walls. In slender RBC cells, on the other hand, away from the horizontal walls, tube-like convection with eddies scaling with the tube diameter and a linear temperature gradient driving the convective flow is present. The crux of our approach is to split the cell into two components: (i) 'wall convection' near the top and bottom horizontal walls and (ii) 'tube convection (TC)' in the central part away from the walls. By applying the scaling relations for both wall convection and TC, and treating the total thermal resistance as a sum of their contributions, unified scaling relations for Nusselt number, Reynolds number and mean vertical temperature gradient in slender RBC cells are developed. Our model is applicable for high enough Rayleigh numbers, such that convection both at the wall and in the tube are turbulent. Our model predictions compare well with the data from various studies in slender RBC cells where these conditions are satisfied. In particular, the effects of Γ and Prandtl number are well captured. We propose a scaled aspect ratio using which we obtain 'universal' correlations for the heat flux and for the fractional temperature drop in the tube that include the effects of Rayleigh and Prandtl numbers. The profiles of suitably scaled horizontal and vertical velocity fluctuations, along with estimates for boundary layer thickness near the horizontal walls, and the radial distribution of the velocity fluctuations in the tube part are also presented.

Key words: turbulent convection, Bénard convection, buoyancy-driven instability

1. Introduction

Natural or free convection or buoyancy-driven flows are caused by differences in temperature, concentration, etc. and are often turbulent, owing to the low viscosities of the most common fluids – air and water. Examples of buoyancy-driven flows in nature include convection in the atmosphere, in clouds, in oceans and in the Earth's mantle. In industry, thermal convection is often encountered in boilers, food processing and chemical industries, cooling of electronic equipment, heat exchangers, HVAC, etc. One of the simplest and widely studied configurations of (natural) thermal convection is Rayleigh–Bénard convection (RBC) (see figure 1*a*) where a layer of fluid sandwiched between two horizontal walls is heated from the bottom and cooled from the top. The forcing responsible for this convection is often expressed non-dimensionally by the Rayleigh number $Ra = g\beta\Delta T H^3/(\nu\alpha)$. Here, β is the thermal expansion coefficient, ν and α are the diffusivities of momentum and temperature, ΔT is the temperature difference between the bottom hot and top cold plates, H is the vertical separation between the plates and g is the acceleration due to gravity. Convection sets in above a critical Rayleigh number of $Ra_{ons} = 1708$ (for laterally unbounded domain), with the formation of laminar convection rolls. With increasing Ra, the flow transitions to unsteady rolls, followed by chaos and finally at high enough Rayleigh numbers, the flow becomes turbulent. Even in the turbulent regime, the flow is characterised by coherent structures: large-scale circulation (LSC) scaling with the height of the cell and sheet-like plumes originating from the top and bottom walls. Almost all the temperature drops occur near the two walls, with the core being nearly isothermal with heat being convected by the LSC offering near-zero thermal resistance.

The variation of the non-dimensional heat flux, Nusselt number Nu, as a function of the forcing Ra is of particular interest. This relation is usually expressed in the form $Nu = CRa^n Pr^p$, where Prandtl number $Pr = \nu/\alpha$ is a fluid property representative of the ratio of diffusivities of momentum and heat. Several scaling relationships based on theoretical arguments or on empirical fits to data from experiments or simulations have been proposed. The so-called 'classical turbulent regime' with the scaling exponent $n = 1/3$ was proposed by the marginal stability argument of Malkus (1954) which was corroborated by some early experiments (Globe & Dropkin 1959). This scaling essentially means that the fluxes are independent of the length scale H, since the entire thermal resistance is localised at the thermal boundary layers at the top and bottom walls which are unaffected by the vertical separation. Later, based on certain assumptions, a slightly smaller exponent of $n = 2/7$ was proposed (Castaing *et al.* 1989; Shraiman & Siggia 1990). In general, datasets from various experiments (Funfschilling *et al.* 2005; Sun *et al.* 2005) for $10^7 \lesssim Ra \lesssim 10^{12}$, known as the hard turbulence regime, generally agree with each other. A scaling exponent of $2/7 \leqslant n \leqslant 1/3$ is generally accepted in this regime, with the scaling exponent slowly changing from $n = 2/7$ at low Ra to $n = 1/3$ at higher Ra. Note that the Prandtl number dependency of Nu is very weak for $Pr \gtrsim 1$ so that p is usually very small (Ahlers, Grossmann & Lohse 2009). In a series of papers (Grossmann & Lohse 2000, 2001; Stevens *et al.* 2013), Grossmann and Lohse suggested that pure power laws may not exist in the entirety of the $Ra-Pr$ parameter space and developed a unified model with a set of implicit equations involving $Nu(Ra, Pr)$ and Reynolds number, $Re(Ra, Pr)$ with certain 'free parameters' that had to be obtained empirically. The central idea was to segregate the volume–averaged kinetic and thermal energy dissipation rates into contributions from the bulk and boundary layers and to demarcate the $Ra-Pr$ parameter space into different regimes based on the relative dominance of these contributions.

At extremely high Rayleigh numbers, beyond some critical value believed to lie between $Ra_u^* \sim 10^{13}$ and 10^{15} (for cells of aspect ratio $\Gamma = d/H \sim 1$), it is expected that there

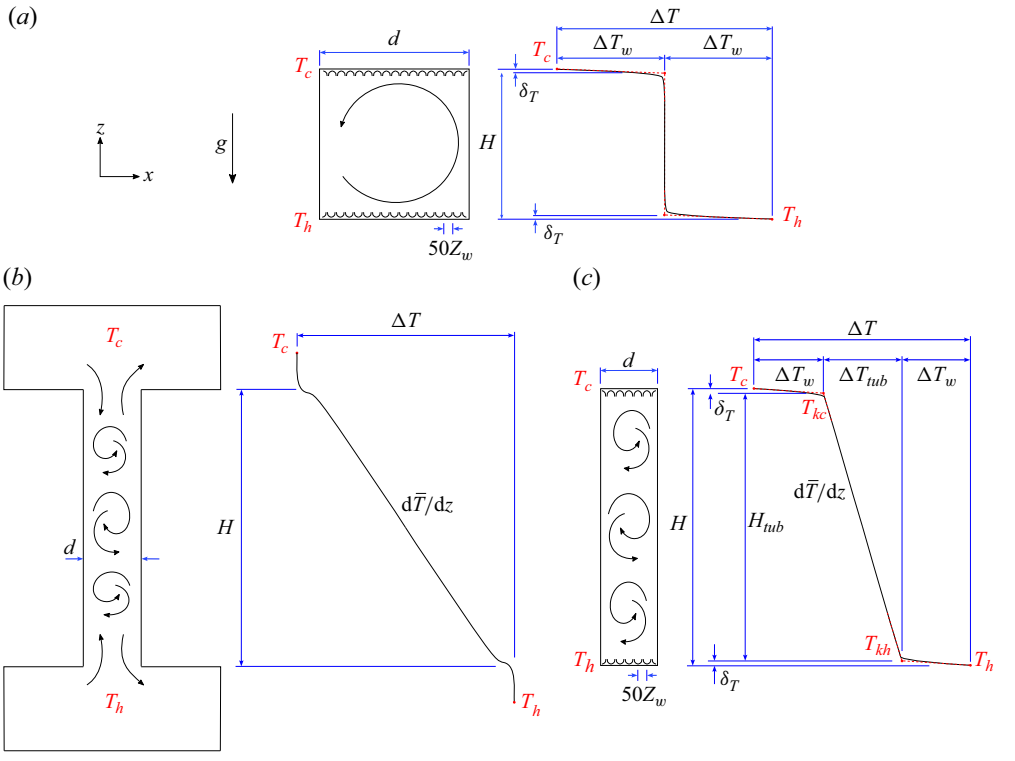

Figure 1. Schematic of (*a*) regular RBC ($\Gamma \sim 1$); (*b*) Tube Convection (TC); and (*c*) slender RBC. For each case, the left-hand side shows a schematic and the right-hand side shows the expected mean temperature profile at high Rayleigh numbers.

will be another transition with a change in value of the scaling exponent n. Kraichnan (1962) predicted that this transition is due to transition to turbulence in the boundary layers and a scaling exponent of $n = 1/2$ would be observed with logarithmic correction in the prefactor. This regime came to be known as the ultimate regime, marking the highest attainable heat transport in a system and the flux and the turbulence intensities becoming independent of the molecular diffusivities (ν and α) of the fluid. There is no consensus on the values of Ra_u^* and of n in the ultimate regime. At very high Rayleigh numbers, while experiments from some groups – Grenoble (Chavanne *et al.* 1997, 2001; Roche *et al.* 2010) and Göttingen (He *et al.* 2012) – have observed evidence of transition to the ultimate regime (mostly with an effective scaling exponent of $n \approx 0.38$ due to logarithmic corrections) above some specific critical Rayleigh numbers, some others – Chicago (Castaing *et al.* 1989; Wu & Libchaber 1992), Eugene/Oregon (Niemela *et al.* 2000; Niemela & Sreenivasan 2006*a*), Trieste (Niemela & Sreenivasan 2003, 2006*b*) and Brno (Urban, Musilová & Skrbek 2011) – do not find any evidence for the transition. The apparent contradiction between different groups of experiments is still debated in the RBC community (Skrbek & Urban 2015; Doering 2020*a*; He *et al.* 2020*b*), and the disparity may be attributed to the fact that at such high Ra, the details of the experimental setup, fluid properties, sidewall conduction effects and aspect ratio seem to matter and the system is extremely sensitive to the boundary conditions (Chilla & Schumacher 2012). In an attempt to reconcile the disparity between different high-Ra experiments, Roche (2020) proposed a phenomenological model in which the transition to the ultimate regime was modelled as a subcritical transition with 'hard turbulence' and 'ultimate regime' branches

that is controlled by the boundary condition details of the RBC cell. Recently, based on the assumption that the velocity and thermal boundary layer thickness are controlled by the dissipation (Kolmogorov and Batchelor) scales outside the boundary layer, Lindborg (2023) proposed that even in the limit of very high Ra, the classical scaling $n = 1/3$ is still valid. For an extensive review of the literature on the subject, the reader is referred to the articles by Siggia (1994), Ahlers *et al.* (2009) and Chilla & Schumacher (2012) and the recent ones by Doering (2020*b*), Sreenivasan & Niemela (2023) and Lohse & Shishkina (2024).

While the debate around the existence of the ultimate regime in regular RBC remains unresolved, the $n = 1/2$ power scaling has been shown to exist in the bulk region by decoupling the bulk flow from the boundary layers, and the convection is driven by a sustained temperature gradient (Lohse & Toschi 2003; Calzavarini *et al.* 2005). Whereas RBC may be considered to be a simple prototype model of natural convection, and has been extensively studied, another equally simple but less studied case is what may be termed as TC (figure 1*b*). In TC, the aspect ratio is small ($\Gamma \leqslant 0.2$) and the bottom and top walls are removed and replaced by two reservoirs. The first experiments to demonstrate TC were performed by Arakeri *et al.* (2000) by connecting a long vertical tube between two reservoirs containing salt and fresh water to create a density difference (essentially making it a high-Prandtl-number convection). With increasing Rayleigh number, the authors reported four different regimes: a half-and-half flow regime with steady exchange flow of uniform unmixed streams; a helical regime where the streams take a helical steady structure; an unsteady laminar regime with unsteady mixing of lighter and heavier fluid; and finally a fully turbulent flow regime where the mixing was completely three-dimensional and random. Subsequent experiments (Cholemari & Arakeri 2005, 2009) characterised some of the salient features of TC in the high-Ra turbulent regime: the existence of a linear mean density gradient along the vertical direction; axially homogeneous turbulence away from the ends; negligible mean velocities; Reynolds shear stress ≈ 0; and the turbulence generated entirely due to buoyancy. Most importantly, $1/2$ power scaling ($Nu \sim Ra^{1/2} Pr^{1/2}$) or the ultimate regime was shown to be easily achievable in TC. Further experiments with similar configurations at Lyon (Gibert *et al.* 2006, 2009; Tisserand *et al.* 2010) and Bangalore (Pawar & Arakeri 2016) and simulations (Schmidt *et al.* 2012) confirmed the existence of such scaling. At Grashof number less than a critical value, a second regime, viscous turbulent regime, was identified with a very different Nusselt number scaling ($Nu \sim Ra^{0.3} Pr^{0.7}$). We discuss these two regimes in TC in detail in § 3.2, but the main point to note is that in both of them, the Nu dependence on Pr is strong, compared with RBC where it is weak.

For RBC, direct numerical simulations (DNS) serve as a viable alternative to experiments; nevertheless, three-dimensional simulations continue to struggle in achieving the expected critical Rayleigh number for the transition to the ultimate regime (Roche 2020). An intelligent workaround would be to cut short the lateral dimensions of the simulation domain, since the Rayleigh number by definition depends only on the vertical size of the domain. Simulations in such slender configurations have been attracting increased attention in the past few years in attempts to reach extreme Rayleigh numbers. Usually, for RBC cells of $\Gamma \gtrsim 1$, the aspect ratio has only a minor effect on the Nu scaling (Ahlers *et al.* 2009). However, some studies (Huang *et al.* 2013; Chong *et al.* 2015; Chong & Xia 2016) have reported that confinement of RBC in one lateral direction (quasi-two-dimensional RBC) can be used to manipulate thermal plumes enhancing the heat transport efficiency. Inspired by this, Hartmann *et al.* (2021) performed DNS of slender RBC cells severely confined both in one or both lateral directions ($1 < \Gamma^{-1} < 64$; $10^7 < Ra < 10^{10}$; $Pr = 4.38$; with rectangular, square and circular cross-sections) to reach

a similar conclusion: moderate confinement in one or both lateral directions can result in slight heat transport enhancement due to formation of vertical coherent plumes; further reduction in Γ from the optimum value resulted in a steep drop in Nu. Subsequently, Shishkina (2021) and Ahlers *et al.* (2022) derived expressions for the critical Ra for the onset of convection as a function of Γ, and showed that when Ra is appropriately re-scaled, the Nu data from various simulations and experiments with different Γ collapse and agree with each other. Further simulations and experiments by Zhang & Xia (2023*a*,*b*) also confirm the slight heat transfer augmentation due to severe lateral confinement. Recently, Iyer *et al.* (2020*a*) performed three-dimensional DNS of RBC in a slender cylindrical domain of $\Gamma = 0.1$ with $Pr = 1$ to cover an extensive range of $Ra = 10^8$–10^{15} and found that the classical scaling $n = 1/3$ holds satisfactorily in the entire range. These are some of the highest Ra achieved in three-dimensional DNS of RBC. Samuel, Samtaney & Verma (2022) performed Large Eddy Simulations (LES) of slender RBC in a cell with a square base over a broad range $10^6 < Ra < 10^{15}$ and found good match of the data with DNS of Iyer *et al.* (2020*a*) with a similar scaling. In subsequent works (Pandey & Sreenivasan 2021; Pandey *et al.* 2022), the Prandtl number dependency was also explored and it was concluded that for $Pr \gtrsim 1$, the Nu scaling in slender cells was close to that in wide cells ($\Gamma \sim 1$), although flow velocities were lower. Once again, there have been debates in the RBC community about the validity of such slender domains to predict the transition to the ultimate state (He *et al.* 2020*a*; Iyer *et al.* 2020*b*).

Despite the emerging attention to convection in slender geometries, there have been no studies (except Ahlers *et al.* 2022) that look into the aspect ratio dependence of heat flux and velocity scalings at such low aspect ratios. In this paper, we look at the RBC problem in such slender geometries with severe confinement in the two lateral directions from a different perspective. We combine the results from TC with those from traditional RBC, and derive the scaling relations for heat transport and velocities in slender RBC cells. The rest of the article is organised as follows. In § 2, we introduce the basic approach of our model and its application to slender RBC. In § 3, we discuss the mechanism of heat transfer and existing scaling relations for turbulent free convection near the walls and tube part of the slender RBC. In § 4, we derive the scaling relations for Nusselt number and temperature gradient in slender RBC along with their aspect ratio and Prandtl number dependence, and compare with some of the recently published data. We discuss the velocity/Reynolds number scaling for slender RBC in § 5. In § 6, we discuss the near-wall variations of the turbulence quantities and compare them with the DNS results of Iyer *et al.* (2020*a*). Finally, we compare the fluxes in a slender RBC cell with those of a TC cell of the same dimensions in § 7. We summarise the work and give our concluding remarks in § 8.

2. Slender RBC

A schematic of a slender RBC cell and the expected mean temperature profile are shown in figure 1(*c*). The width or diameter of the cell d is much smaller compared with the height of the cell H, so that the aspect ratio $\Gamma = d/H \ll 1$. Total temperature difference between the bottom hot (T_h) and top cold (T_c) plates is $\Delta T = T_h - T_c$. The sidewalls are assumed to be adiabatic. The governing parameters are Rayleigh number $Ra = g\beta\Delta T H^3/(\nu\alpha)$, aspect ratio Γ and Prandtl number Pr. For slender RBC, an alternative Rayleigh number based on d is sometimes more convenient, $Ra_d = g\beta\Delta T d^3/(\nu\alpha) = Ra\Gamma^3$. The non-dimensional heat flux $Nu = q''/q''_{cond} = q''H/(k\Delta T)$ will depend on the three parameters $Nu = f(Ra \text{ or } Ra_d, \Gamma, Pr)$. Here q'' is the total heat flux across any horizontal cross-section (which is also equal to the conductive heat flux at the walls), q''_{cond} is the

hypothetical conductive flux across the height of the cell in the absence of any fluid motion and k is the thermal conductivity of the fluid. The purpose of this paper is to propose a model that gives Nu as a function of the three parameters, for $\Gamma \ll 1$ and for high enough Ra when the convection is turbulent.

At high enough Rayleigh numbers, the mean temperature profile $\overline{T}(z)$ can be considered to have two parts – two temperature drops near the two horizontal walls, and a linear variation (Iyer *et al.* 2020*a*; Pandey & Sreenivasan 2021) over much of the central height of the cell (see figure 1*c*). This is in contrast to what is observed in regular RBC ($\Gamma \gtrsim 1$), where similar temperature drops are observed at the walls, but the core is essentially isothermal (figure 1*a*). Figure 1(*b*) shows a schematic of TC, that which occurs in a long vertical tube separated by two tanks containing heavier and lighter fluid at the top and bottom, respectively. The density difference can be created by species concentration difference (e.g. brine and fresh water (Cholemari & Arakeri 2005), when $Pr \sim 600$) or by temperature difference ($Pr \sim 6$) (Pawar 2015). When $L/d \gg 1$, the (unstable) density gradient is necessarily linear, and the convection is axially homogeneous with eddies scaling with tube diameter at the higher range of Ra in which our model is applicable. In slender RBC, the part where the temperature varies linearly is akin to TC, where the flow is axially homogeneous.

The approach we take to model slender RBC, or confined convection, is to break up the convection into two parts, the wall part and the tube part. These two parts offer different resistances to the heat flow; the heat flux is determined by the sum of these resistances in series. We use known correlations for the wall and tube parts. Our model works for certain ranges of Rayleigh numbers and aspect ratios, for which these correlations are valid.

The heat flux in slender RBC is determined by three thermal resistances in series, two at the two walls (both equal to R_w) and the other in the tube (R_{tub}):

$$q'' = \frac{\Delta T}{R_{tot}} = \frac{\Delta T_w}{R_w}\bigg|_{bot} = \frac{\Delta T_{tub}}{R_{tub}} = \frac{\Delta T_w}{R_w}\bigg|_{top}, \tag{2.1}$$

where R_{tot} is the total thermal resistance. The temperature drops at the top ($\Delta T_h = T_h - T_{kh}$) and bottom ($\Delta T_c = T_{kc} - T_c$) walls are assumed to be equal due to symmetry so that $\Delta T_h = \Delta T_c = \Delta T_w$, where ΔT_w is the mean temperature drop at either wall. Here T_{kh} and T_{kc} are the 'knee' temperatures near the bottom and top walls, respectively (see figure 1*c*). The total temperature difference ΔT is thus the sum of the temperature drops at the two walls (ΔT_w) and in the tube part ($\Delta T_{tub} = T_{kh} - T_{kc}$):

$$\Delta T = \Delta T_h + \Delta T_{tub} + \Delta T_c = 2\Delta T_w + \Delta T_{tub}. \tag{2.2}$$

We use the correlations at the wall and in the tube to determine ΔT_w and ΔT_{tub}, and R_w and R_{tub}. The linear variation of the mean temperature in the tube part is $(\mathrm{d}\overline{T}/\mathrm{d}z)|_{tube} = \Delta T_{tub}/H_{tub}$, where $H_{tub} = H - 2\delta_T$ is the height which has the linear temperature gradient. For rest of the paper, we suppress the subscript 'tube' for the temperature gradients so that $(\mathrm{d}\overline{T}/\mathrm{d}z)|_{tube} \equiv (\mathrm{d}\overline{T}/\mathrm{d}z)$, with the understanding that temperature gradients are of the tube part, unless otherwise stated. Since the thermal boundary layer thickness $\delta_T \ll H$, $H_{tub} \approx H$ and the temperature gradient in the tube may be approximated as

$$\frac{\mathrm{d}\overline{T}}{\mathrm{d}z} = \frac{\Delta T_{tub}}{H}. \tag{2.3}$$

Parameter	Definition	Remarks
Ra	$g\beta\Delta T H^3/(\nu\alpha)$	Conventional Rayleigh number based on total height
Ra_d	$g\beta\Delta T d^3/(\nu\alpha)$	Rayleigh number based on cell width
Ra_w	$g\beta\Delta T_w d^3/(\nu\alpha)$	Rayleigh number at the walls
Ra_g	$g\beta\frac{\mathrm{d}\overline{T}}{\mathrm{d}z}d^4/(\nu\alpha)$	Gradient Rayleigh number in the tube
Ra_{δ_T}	$g\beta\Delta T_w\delta_T^3/(\nu\alpha)$	Rayleigh number based on thermal boundary layer thickness
Ra_{λ_p}	$g\beta\Delta T_w\lambda_p^3/(\nu\alpha)$	Rayleigh number based on plume spacing λ_p
$\mathrm{d}\widetilde{T}/\mathrm{d}\tilde{z}$	$\frac{\mathrm{d}\overline{T}}{\mathrm{d}z}\left(\frac{\Delta T}{H}\right)^{-1}$	Non-dimensional temperature gradient in the tube; also the ratio of temperature drop in the tube to the total temperature difference ($=\Delta T_{tub}/\Delta T$)
Nu	$q''H/(k\Delta T)$	Conventional Nusselt number
C_{q_w}	$Ra_{\delta_T}^{-1/3}$	Alternative non-dimensional heat transfer coefficient at the walls
Nu_g	$q''/\left(k\frac{\mathrm{d}\overline{T}}{\mathrm{d}z}\right)$	Gradient Nusselt number in the tube
Re	$u_{rms}H/\nu$	Conventional Reynolds number based on r.m.s. velocity and total height
Re_d	$u_{rms}d/\nu$	Reynolds number based on r.m.s. velocity and cell width

Table 1. List of some non-dimensional parameters relevant to slender RBC.

We may non-dimensionalise the temperature as $\widetilde{T}=(\overline{T}-T_c)/\Delta T$ and height as $\tilde{z}=z/H$. The dimensionless temperature gradient in the tube is thus given by

$$\frac{\mathrm{d}\widetilde{T}}{\mathrm{d}\tilde{z}}=\frac{\mathrm{d}\overline{T}}{\mathrm{d}z}\left(\frac{\Delta T}{H}\right)^{-1}=\frac{\Delta T_{tub}}{\Delta T}. \tag{2.4}$$

Since $\Delta T_w=(\Delta T-\Delta T_{tub})/2$, using (2.4) we may write

$$\frac{\Delta T_w}{\Delta T}=\frac{1}{2}\left(1-\frac{\mathrm{d}\widetilde{T}}{\mathrm{d}\tilde{z}}\right). \tag{2.5}$$

It is sometimes useful to define a wall Rayleigh number based on the temperature jump at the wall ΔT_w and the width (or diameter) of the cell d as $Ra_w=g\beta\Delta T_w d^3/(\nu\alpha)$. This definition comes in handy in our analysis of the slender RBC especially when dealing with the near-wall dynamics of plumes and the boundary layer, as we shall see later. The wall Rayleigh number Ra_w can be expressed in terms of Ra using (2.5) as

$$Ra_w=\frac{1}{2}Ra\left(1-\frac{\mathrm{d}\widetilde{T}}{\mathrm{d}\tilde{z}}\right)\Gamma^3=\frac{1}{2}Ra_d\left(1-\frac{\mathrm{d}\widetilde{T}}{\mathrm{d}\tilde{z}}\right). \tag{2.6}$$

Note that for a regular RBC with $\Gamma\sim 1$, $Ra_d\approx Ra$ and either can be used interchangeably. For slender RBC, Ra_d can be perceived as an equivalent Rayleigh number of a regular RBC with domain height d instead of H. Definitions of some of the non-dimensional parameters discussed in this section along with some that are introduced in the subsequent sections are given in table 1 for quick reference.

3. Heat transport in a slender RBC cell

Having set some of the basic definitions, we now proceed to analyse the heat transport in a slender RBC cell. The time-averaged heat flux is same at all horizontal cross-sections, and the temperature drops at the (top and bottom) walls and in the tube part are determined by the thermal resistance offered by each.

3.1. *Thermal resistance at the walls*

The temperature drop at the wall ΔT_w in RBC occurs across the thermal boundary layer thickness, which is defined as $\delta_T = \Delta T_w/(\mathrm{d}\overline{T}/\mathrm{d}z)|_w$, where $(\mathrm{d}\overline{T}/\mathrm{d}z)|_w$ is the mean temperature gradient at the wall. Thus, $\delta_T/H = (\Delta T_w/\Delta T)Nu^{-1}$. For turbulent convection in a regular RBC cell with a nearly isothermal core, $\Delta T_w = \Delta T/2$ and $\delta_T/H = (1/2)Nu^{-1}$. However, for a slender RBC cell, we need to account for the drop in the tube part. Using (2.5), the thermal boundary layer thickness for slender RBC can be written as

$$\frac{\delta_T}{H} = \frac{1}{2}\left(1 - \frac{\mathrm{d}\widetilde{T}}{\mathrm{d}\tilde{z}}\right) Nu^{-1}. \tag{3.1}$$

To obtain the resistance at the walls, we use the correlations for heat flux in classical RBC ($\Gamma \gtrsim 1$). Instead of Nusselt number Nu, however, we use an alternative parameter as proposed by Theerthan & Arakeri (2000) to non-dimensionalise the heat flux, which is more convenient and meaningful:

$$C_{q_w} = \frac{q''}{k\Delta T_w}\left(\frac{g\beta}{\nu\alpha}\Delta T_w\right)^{-1/3} = Ra_{\delta_T}^{-1/3}. \tag{3.2}$$

This proposal is an outcome of the observation that in turbulent natural convection, Nu scales roughly as $Ra^{1/3}$, making the heat flux nearly independent of the length scale. By assuming the heat flux to be dependent only on ΔT_w, the temperature difference across the wall boundary layer, and the fluid properties, dimensional analysis gives the above expression for C_{q_w}. It turns out that $C_{q_w} = Ra_{\delta_T}^{-1/3}$, where $Ra_{\delta_T} = g\beta\Delta T_w\delta_T^3/(\nu\alpha)$ is the Rayleigh number based on conduction-layer thickness δ_T. The advantage of such a representation is the fact that unlike Nu which changes by orders of magnitude with changing Ra, the value of C_{q_w} lies between 0.1 to 0.3 not just for RBC, but for various configurations (see Arakeri 2012; Arakeri, Kumar & Mahapatra 2024) involving natural convection in the presence of a wall. The heat flux $q'' = k(\mathrm{d}\overline{T}/\mathrm{d}z)|_w = k\Delta T_w/\delta_T$ in terms of C_{q_w} is thus given by

$$q'' = C_{q_w}k\left(\frac{g\beta}{\nu\alpha}\right)^{1/3}\Delta T_w^{4/3}. \tag{3.3}$$

In 'standard' RBC ($\Gamma \gtrsim 1$) since $\Delta T_w \approx \Delta T/2$, using (3.3) we get an expression for C_{q_w} in terms of Nu and Ra as $C_{q_w} = 2^{4/3}NuRa^{-1/3}$. Using the usual representation of scaling for RBC, $Nu = CRa^nPr^p$, we can obtain $C_{q_w} = 2^{4/3}CRa^{n-1/3}Pr^p$. For the classical scaling regime ($n = 1/3$), we get $C_{q_w} = 2^{4/3}CPr^p$; C_{q_w} is only a function of Pr and not Ra. For example, the scaling proposed by Globe & Dropkin (1959), $Nu = 0.069Ra^{1/3}Pr^{0.074}$ gives $C_{q_w} = 0.1739Pr^{0.074}$. Note that C_{q_w} is not just a compensated Nusselt number, it is a different and more suitable non-dimensional measure of heat flux than Nu. The physical significance of C_{q_w} is the fact that $C_{q_w} = $ const. implies that for different Ra, the conduction layer thickness δ_T adjusts itself to compensate for the temperature difference across it (ΔT_w) to keep Ra_{δ_T} a constant, which fits in with the argument of Malkus (1954) and forms the basis for the models for turbulent RBC by Howard (1966) and Theerthan & Arakeri (1998). For more discussion on C_{q_w} and its advantages, the reader is referred to Theerthan & Arakeri (2000), Puthenveettil & Arakeri (2005), Arakeri (2012) and Arakeri *et al.* (2024).

For free convection over heated horizontal flat plates, at high enough Rayleigh numbers $Nu = 0.15Ra_w^{1/3}$ for $8 \times 10^6 < Ra_w < 1.6 \times 10^9$ (Lloyd & Moran 1974) with the length scale equal to the width of the plate d and temperature scale ΔT_w as the temperature

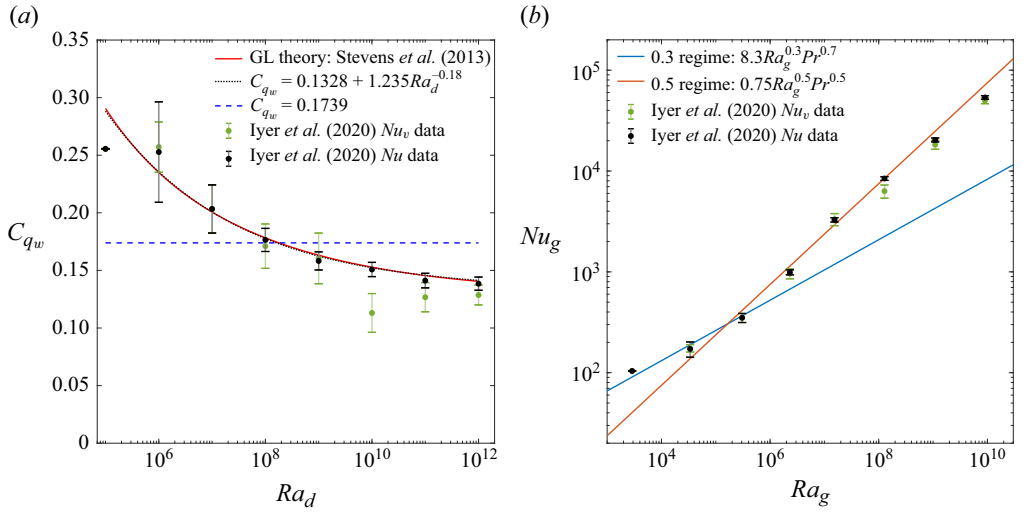

Figure 2. (*a*) Variation of the dimensionless wall heat transfer coefficient C_{q_w} with $Ra_d = Ra\Gamma^3$ in a slender RBC cell, calculated using (3.4) for Iyer *et al.* (2020*a*) ($\Gamma = 0.1$ and $Pr = 1$). Red curve shows C_{q_w} calculated from the Grossmann–Lohse (GL) theory (Stevens *et al.* 2013) for regular RBC with $\Gamma = 1$, $Pr = 1$ and black dotted line is the corresponding least-squares fit given by $C_{q_w} = 0.1328 + 1.235Ra_d^{-0.18}$. Blue dashed line shows a constant $C_{q_w} = 0.1739$ approximation from Globe & Dropkin (1959). (*b*) Scaling of gradient-based dimensionless quantities Nu_g versus Ra_g in the tube region of Iyer *et al.* (2020*a*), calculated using (3.5) and (3.6) and compared with the two regimes of scaling in Pawar & Arakeri (2016). In both panels, the data from Iyer *et al.* (2020*a*) are calculated from Nusselt number averaged at the top/bottom plates Nu (black markers) and that averaged in the whole volume Nu_v (light-green markers).

difference between the plate and the ambient. From this correlation, we get $C_{q_w} = 0.15$. In both the above examples, the $Nu-Ra$ scaling laws follow the classical 1/3 power law which gives a constant value (with a weak function of Pr) for C_{q_w}. For a non-classical scaling, for example, $Nu = 0.15Ra^{0.29}$ for $Pr = 0.7$ in a RBC container of $\Gamma = 1$ (Scheel & Schumacher 2017), we obtain $C_{q_w} = 0.378Ra^{-0.0433}$, a weak function of Ra.

We next check the values of C_{q_w} obtained in the slender RBC cell using the Nu versus Ra data presented in Iyer *et al.* (2020*a*). For a slender RBC cell, using (2.5) in (3.3) the expression for C_{q_w} becomes

$$C_{q_w} = Ra_{\delta_T}^{-1/3} = 2^{4/3} Nu\, Ra^{-1/3} \left(1 - \frac{\mathrm{d}\widetilde{T}}{\mathrm{d}\tilde{z}}\right)^{-4/3}. \tag{3.4}$$

The values of C_{q_w} so calculated for slender RBC with $\Gamma = 0.1$ and $Pr = 1$ from Iyer *et al.* (2020*a*) data are shown in figure 2(*a*) and plotted against $Ra_d = Ra\Gamma^3$. Two versions of C_{q_w} are shown: one calculated from Nusselt number averaged over the top/bottom walls (Nu) and other averaged in the whole domain (Nu_v). To compare this with that of a regular RBC, we show for a cell with $\Gamma = 1$ and $Pr = 1$, the C_{q_w} prediction from the GL theory with the updated prefactors (Stevens *et al.* 2013). A least-squares curve fit to the GL curve gives $C_{q_w} = 0.1328 + 1.235Ra_d^{-0.18}$ for $Pr = 1$. Ideally, we should be using Ra_w instead of Ra_d for comparing the C_{q_w} values for regular and slender RBC cases, because ΔT_w is the forcing at the wall and not ΔT as is assumed in the figure. However, $Ra_d = 2Ra_w(1 - (\mathrm{d}\widetilde{T}/\mathrm{d}\tilde{z})^{-1}$ and for the cases we are considering, the values of $\mathrm{d}\widetilde{T}/\mathrm{d}\tilde{z}$ are small, and since C_{q_w} is a very weak function of Ra_w, the plot of C_{q_w} versus Ra_w closely resembles that of C_{q_w} versus Ra_d. It can be seen that both versions (from Nu and Nu_v) of the Iyer *et al.*

(2020*a*) data follow the prediction of GL theory very closely, validating our hypothesis that the heat transfer mechanism at the walls of both regular and slender RBC cells is the same. Also shown is the constant approximation of $C_{q_w} = 0.1739$ based on the Globe & Dropkin (1959) fit for reference. The main conclusion is that heat transfer at the walls of slender RBC is conveniently obtained by using the non-dimensional heat transfer measure C_{q_w}, whose value is nearly constant.

3.2. *Thermal resistance in the tube part*

Convection in the tube part of the slender RBC cell, which we term as TC, has a very different character compared with the convection near the walls. At high enough Rayleigh numbers the flow is axially homogeneous and the turbulence is entirely buoyancy-driven (Cholemari & Arakeri 2009).

A conventional definition of Rayleigh number for the tube part would be given by $Ra_{tub} = g\beta\Delta T_{tub} H^3/(\nu\alpha)$, where T_{tub} is the difference between the knee temperatures at the tube ends. However, since the convection is axially homogeneous and driven by a linear temperature gradient, it is more appropriate to use what we call the gradient-based Rayleigh number (Arakeri *et al.* 2000), based on the vertical temperature gradient in the tube and the tube diameter: $Ra_g = g\beta\Delta T_d d^3/(\nu\alpha) = g\beta(\mathrm{d}\overline{T}/\mathrm{d}z)d^4/(\nu\alpha)$, where $\Delta T_d = (\mathrm{d}\overline{T}/\mathrm{d}z)d$ is the temperature difference in the tube part over a diameter height. Essentially, away from the top and bottom ends, the convection is driven by the local temperature gradient and the length scale is the tube diameter (Cholemari & Arakeri 2005, 2009). The relation between Ra_g and Ra in slender RBC is obtained using (2.3) and (2.4) as

$$Ra_g = Ra\left(\frac{\mathrm{d}\widetilde{T}}{\mathrm{d}\tilde{z}}\right)\Gamma^4. \tag{3.5}$$

Again, for the tube part of slender RBC, a gradient-based Nusselt number can be defined as $Nu_g = q''d/k\Delta T_d = q''/(k(\mathrm{d}\overline{T}/\mathrm{d}z))$ which depends only on the local temperature gradient in the tube. Taking the ratio Nu_g/Nu and using (2.4), we have

$$Nu_g = Nu\left(\frac{\mathrm{d}\widetilde{T}}{\mathrm{d}\tilde{z}}\right)^{-1}. \tag{3.6}$$

A general scaling relation for heat flux in the tube region may be written as

$$Nu_g = C_{tub} Ra_g^a Pr^b. \tag{3.7}$$

Several regimes, depending on Ra_g and Pr, exist in TC. Some have been documented for high Pr in Arakeri *et al.* (2000). At high enough Ra_g, the convection becomes turbulent with no mean flow. For the turbulent flow itself, two regimes have been identified (Pawar & Arakeri 2016). Combining all the experimental and numerical data that were reported until then at different Prandtl numbers, Pawar & Arakeri (2016) argued that the correlations for the two turbulent regimes are best given in terms of the gradient-based Grashof number $Gr_g = g\beta(\mathrm{d}\overline{T}/\mathrm{d}z)d^4/\nu^2 = Ra_g/Pr$, and proposed for the two regimes the following relations:

$$Nu_g = C_{0.3} Gr_g^{0.3} Pr = C_{0.3} Ra_g^{0.3} Pr^{0.7} \quad \text{for } Gr_{g0} < Gr_g < Gr_{gc}, \tag{3.8a}$$

$$Nu_g = C_{0.5} Gr_g^{0.5} Pr = C_{0.5} Ra_g^{0.5} Pr^{0.5} \quad \text{for } Gr_g > Gr_{gc}, \tag{3.8b}$$

where $Gr_{gc} \simeq 1.6 \times 10^5$ is the critical gradient Grashof number where the flow transitions from 0.3 to 0.5 power regime and Gr_{g0} is a possible unknown lower critical limit below which the scaling is unexplored. The empirically determined values for the prefactors

Ra	10^8	10^9	10^{10}	10^{11}	10^{12}	10^{13}	10^{14}	10^{15}
$\frac{d\tilde{T}}{d\tilde{z}}$	0.2877	0.3369	0.3051	0.2310	0.1533	0.1275	0.1095	0.0903
Ra_d	10^5	10^6	10^7	10^8	10^9	10^{10}	10^{11}	10^{12}
Ra_w	3.56×10^4	3.32×10^5	3.47×10^6	3.85×10^7	4.23×10^8	4.36×10^9	4.45×10^{10}	4.55×10^{11}
Ra_g	2.88×10^3	3.37×10^4	3.05×10^5	2.31×10^6	1.53×10^7	1.28×10^8	1.10×10^9	9.03×10^9
Nu	29.94 ±0.04	58 ±10	107 ±11	229 ±13	503 ±25	1075 ±44	2228 ±100	4845 ±200
Nu_v	29.94 ±0.01	59 ±5	107 ±11	222 ±25	510 ±70	806 ±120	2000 ±200	4500 ±300
$C_{q_{w,s}}$	0.2555 ±0.0003	0.2528 ±0.0436	0.2033 ±0.0209	0.1765 ±0.0100	0.1582 ±0.0079	0.1508 ±0.0062	0.1412 ±0.0063	0.1385 ±0.0057
$C_{q_{w,v}}$	0.2555 ±0.0001	0.2571 ±0.0218	0.2033 ±0.0209	0.1711 ±0.0193	0.1604 ±0.0220	0.1131 ±0.0168	0.1267 ±0.0127	0.1286 ±0.0086
$Nu_{g,s}$	$(1.04\pm0.00)\times10^2$	$(1.72\pm0.30)\times10^2$	$(3.51\pm0.36)\times10^2$	$(9.91\pm0.56)\times10^2$	$(3.28\pm0.16)\times10^3$	$(8.43\pm0.35)\times10^3$	$(2.03\pm0.09)\times10^4$	$(5.37\pm0.22)\times10^4$
$Nu_{g,v}$	$(1.04\pm0.00)\times10^2$	$(1.75\pm0.15)\times10^2$	$(3.51\pm0.36)\times10^2$	$(9.61\pm1.08)\times10^2$	$(3.33\pm0.46)\times10^3$	$(6.32\pm0.94)\times10^3$	$(1.83\pm0.18)\times10^4$	$(4.98\pm0.33)\times10^4$
Re_d	6.01×10^1	1.92×10^2	5.57×10^2	1.70×10^3	5.25×10^3	1.33×10^4	4.10×10^4	1.09×10^5
λ_p/d	1.5805	0.7513	0.3433	0.1541	0.0693	0.0318	0.0147	0.0068
d/λ_p	0.63	1.33	2.91	6.49	14.4	31.4	68.1	147.9

Table 2. Summary of different non-dimensional parameters at different Ra calculated for Iyer *et al.* (2020*a*) data ($Pr = 1$, $\Gamma = 0.1$). The subscripts s and v are used to represent quantities calculated from the Nusselt number data of the reference evaluated at the top/bottom plates (Nu) and evaluated in the domain volume (Nu_v), respectively.

are $C_{0.3} = 8.3 \pm 3$ and $C_{0.5} = 0.75 \pm 0.1$. The scaling exponents in (3.7) take the values $a = 0.3$, $b = 0.7$ for the 0.3 regime ($Gr_g < Gr_{gc}$) and $a = 0.5$, $b = 0.5$ for the 0.5 regime ($Gr_g > Gr_{gc}$).

The 0.5 regime ($Gr_g > Gr_{gc}$) corresponds to the 'ultimate regime' where heat flux becomes independent of the viscosity and thermal diffusivity of the fluid, and is easily and unambiguously achievable with ordinary fluids at laboratory scales in TC as compared with RBC. For the 0.3 regime ($Gr_g < Gr_{gc}$), it was shown (Pawar & Arakeri 2016) that viscous effects start affecting the flux, and we obtain a 'viscous turbulent' regime in TC. It is important to note that the nature of the correlations is very different from those for regular RBC, in particular the dependence on Pr is strong.

The plot of Nu_g versus Ra_g (figure 2*b*) shows that the data from Iyer *et al.* (2020*a*) closely follow the TC correlations ((3.8*a*), (3.8*b*)), including the flow transitioning from 0.3 to 0.5 regime at the critical gradient Grashof number Gr_{gc}. Equations (3.5) and (3.6) were used to calculate Nu_g and Ra_g from the simulation data (from both versions of Nusselt number, Nu and Nu_v). The close match between data and prediction validates our hypothesis that the flow in the tube part of the slender RBC is very similar to or the same as that in TC.

The values of all the non-dimensional parameters calculated for the simulations of Iyer *et al.* (2020*a*) at $Pr = 1$ and $\Gamma = 0.1$ are given in table 2. The equations used for $d\tilde{T}/d\tilde{z}$, Ra_w, C_{q_w}, Ra_g and Nu_g have been discussed in §§ 2 and 3. The calculation of Reynolds number Re_d and the mean plume spacing λ_p/d are discussed later in the paper.

4. Correlations for heat flux in slender RBC

In this section, we combine the scaling relations for the wall and the tube parts to derive a generalised Nusselt–Rayleigh scaling relation for slender RBC. The total temperature drop is $\Delta T = 2\Delta T_w + \Delta T_{tub}$ (2.2); and we use the correlation for the wall part to calculate ΔT_w

and that for the tube part to calculate ΔT_{tub}. The temperature drops are directly related to the relative resistances in each of the two parts.

Equation (3.3) gives the relation between heat flux q'' and temperature drop at the wall ΔT_w in terms of C_{q_w}. We may invert this relation and write

$$\Delta T_w = C_{q_w}^{-3/4} \left(\frac{q''}{k}\right)^{3/4} \left(\frac{g\beta}{\nu\alpha}\right)^{-1/4} = K_w^{-3/4} (q'')^{3/4}, \tag{4.1}$$

where $K_w = C_{q_w} \rho c_p (g\beta)^{1/3} \nu^{-1/3} \alpha^{2/3}$, a temporary constant.

The general scaling law for TC is given by (3.7). Using the definitions of Nu_g, Ra_g and Pr in this, we have

$$\frac{q''}{k\frac{\mathrm{d}\overline{T}}{\mathrm{d}z}} = C_{tub} \left(\frac{g\beta\frac{\mathrm{d}\overline{T}}{\mathrm{d}z} d^4}{\nu\alpha}\right)^a \left(\frac{\nu}{\alpha}\right)^b. \tag{4.2}$$

Using (2.3) and $\Gamma = d/H$ and rearranging, we have

$$q'' = C_{tub} \rho c_p (g\beta)^a \nu^{b-a} \alpha^{1-a-b} \Gamma^{4a} H^{3a-1} {\Delta T_{tub}}^{1+a}. \tag{4.3}$$

Inverting this relation, we have

$$\Delta T_{tub} = K_{tub}^{\frac{-1}{1+a}} (q'')^{\frac{1}{1+a}} \Gamma^{\frac{-4a}{1+a}} H^{\frac{1-3a}{1+a}}, \tag{4.4}$$

where $K_{tub} = C_{tub} \rho c_p (g\beta)^a \nu^{b-a} \alpha^{1-a-b}$, another temporary constant.

4.1. *The generalised Nu–Ra correlation for slender RBC*

Substituting (4.1) and (4.4) to (2.2), we get

$$\Delta T = 2K_w^{-3/4} (q'')^{3/4} + K_{tub}^{\frac{-1}{1+a}} (q'')^{\frac{1}{1+a}} \Gamma^{\frac{-4a}{1+a}} H^{\frac{1-3a}{1+a}}. \tag{4.5}$$

We can non-dimensionalise this equation by multiplying throughout by $(g\beta/\nu\alpha)H^3$:

$$\frac{g\beta\Delta T H^3}{\nu\alpha} = 2\left(\frac{g\beta}{\nu\alpha}\right) K_w^{-3/4} (q'')^{3/4} H^3 + \left(\frac{g\beta}{\nu\alpha}\right) K_{tub}^{\frac{-1}{1+a}} (q'')^{\frac{1}{1+a}} \Gamma^{\frac{-4a}{1+a}} H^{\frac{1-3a}{1+a}} H^3. \tag{4.6}$$

Substituting for K_w and K_{tub} and rearranging terms:

$$\begin{aligned} \frac{g\beta\Delta T H^3}{\nu\alpha} = {} & 2C_{q_w}^{-3/4} \left(\frac{g\beta\Delta T H^3}{\nu\alpha}\right)^{3/4} \left(\frac{q'' H}{k\Delta T}\right)^{3/4} \\ & + C_{tub}^{\frac{-1}{1+a}} \left(\frac{g\beta\Delta T H^3}{\nu\alpha}\right)^{\frac{1}{1+a}} \left(\frac{q'' H}{k\Delta T}\right)^{\frac{1}{1+a}} \left(\frac{\nu}{\alpha}\right)^{\frac{-b}{1+a}} \Gamma^{\frac{-4a}{1+a}}. \end{aligned} \tag{4.7}$$

Thus, we have the generalised *Nu–Ra* correlation for slender RBC cells as

$$2C_{q_w}^{-3/4} Nu^{3/4} Ra^{3/4} + C_{tub}^{\frac{-1}{1+a}} Nu^{\frac{1}{1+a}} Ra^{\frac{1}{1+a}} Pr^{\frac{-b}{1+a}} \Gamma^{\frac{-4a}{1+a}} = Ra. \tag{4.8}$$

Instead of the familiar power-law form, we have an implicit equation between Nu, Ra, Pr and Γ. The first term on the left-hand side corresponds to the wall part and second term corresponds to the tube part. Due to the implicit nature of the equation, the Nu value has to be calculated iteratively. The values of C_{tub}, a and b depend on the regime of TC scaling in the tube part of the slender RBC. For the two regimes for the tube part mentioned

in (3.8), (4.8) becomes

$$2C_{q_w}^{-3/4}Nu^{3/4}Ra^{3/4} + C_{0.3}^{-10/13}Nu^{10/13}Ra^{10/13}Pr^{-7/13}\Gamma^{-12/13} = Ra \quad \text{for } Gr_{g0} < Gr_g < Gr_{gc}, \tag{4.9a}$$

$$2C_{q_w}^{-3/4}Nu^{3/4}Ra^{3/4} + C_{0.5}^{-2/3}Nu^{2/3}Ra^{2/3}Pr^{-1/3}\Gamma^{-4/3} = Ra \quad \text{for } Gr_g > Gr_{gc}, \tag{4.9b}$$

where $C_{tub} = C_{0.3}$, $a = 0.3$, $b = 0.7$ for the 0.3 regime and $C_{tub} = C_{0.5}$, $a = b = 0.5$ for the 0.5 regime. Depending on whether the gradient-based Grashof number Gr_g in the tube part of the slender RBC cell is below or above the critical value $Gr_{gc} = 1.6 \times 10^5$, one has to solve either (4.9*a*) or (4.9*b*) to obtain Nu at a particular Ra, Pr and Γ. In order to determine the regime into which the convection in the tube part falls, we need to know the value of Gr_g, which is unknown *a priori*. Hence, we need to find the critical Grashof number Gr_c (or the critical Rayleigh number Ra_c) based on the total temperature difference and cell height when the convection regime in the tube part changes from the 0.3 to 0.5 regime. The procedure to determine Gr_c or Ra_c is given in Appendix A.

4.2. *Comparison of model predictions with data*

Next, we explore the validity of our model by comparing it against some of the recent studies involving convection in slender cells. We use only those data from the different studies that satisfy the restrictions on Ra placed by our model. We will see that in several cases, the flow was not 'turbulent' in the tube or at the wall or both, and thus did not satisfy the conditions required by the model.

The variation of Nu (compensated by $Ra^{1/3}$) with Ra for a slender RBC cell of aspect ratio $\Gamma = 0.1$ and $Pr = 1$ obtained using (4.9*a*) and (4.9*b*) is shown in figure 3(*a*). The Nusselt number data from Iyer *et al.* (2020*a*) (both versions, Nu and Nu_v along with the corresponding error bars) and the data-fit proposed by them are shown, along with the LES results of Samuel *et al.* (2022) for the same Rayleigh numbers and conditions ($\Gamma = 0.1$, $Pr = 1$). We note here that the wall heat flux values from Iyer *et al.* (2020*a*) may not be fully converged for $Ra > 10^{13}$, but it it is unlikely that the converged values will be significantly different. The differences in the Nu and Nu_v data, as well as between the two studies, highlight the challenges in simulations at these extreme Rayleigh numbers. The blue and red curves correspond to the predictions using the current model with a constant ($C_{q_w} = 0.1739$ from the Globe & Dropkin (1959) fit) and variable ($C_{q_w} = 0.1328 + 1.235Ra_d^{-0.18}$ from GL theory) approximations for C_{q_w}, respectively. For this configuration, the value of the critical Rayleigh number where the regime changes in the tube part is determined to be $Ra_c \approx 5.3 \times 10^9$ (see Appendix A). Below the critical Rayleigh number (the exact value of which depends very weakly on the choice of C_{q_w}), (4.9*a*) corresponding to the 0.3 regime is used, and above which (4.9*b*) corresponding to the 0.5 power regime is used. Also shown are some other well-known correlations in the literature for RBC, none of which fit well with the slender RBC data. The classical scaling relation given by Globe & Dropkin (1959) and the fit proposed by Iyer *et al.* (2020*a*) appear as horizontal lines in the compensated plot. We may mention that the predictions using the classical RBC correlations become worse as the cells become taller, as Γ reduces. It can be seen that while our model with the constant C_{q_w} approximation does not faithfully reproduce the given trend of data points, the model with variable C_{q_w} approximation follows the data remarkably well. It should be noted that even with the constant $C_{q_w} = 0.1739$ approximation, the error in the estimate is less that 20 %. In fact, a $C_{q_w} = 0.15$ approximation (from the horizontal flat plate) gives a better

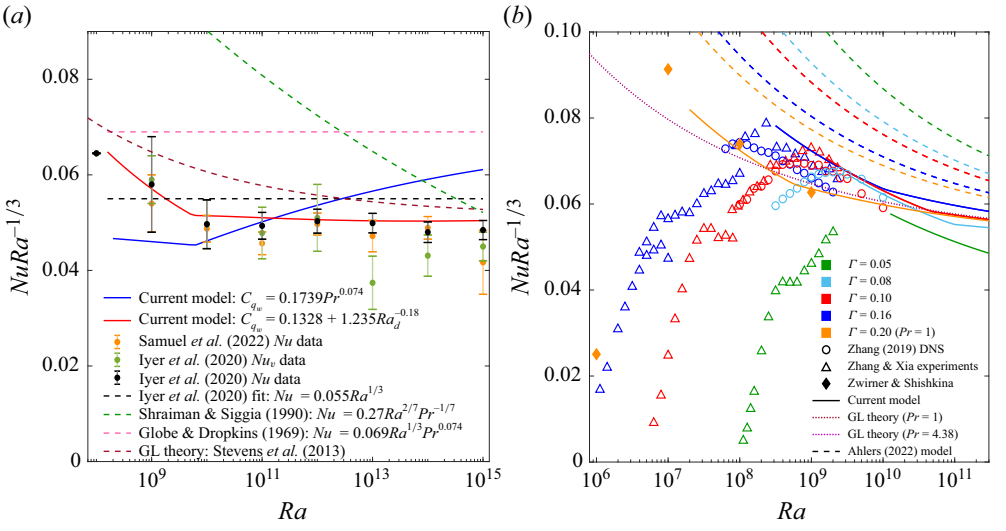

Figure 3. (*a*) Compensated Nu versus Ra for slender RBC using the current model (4.9) at $\Gamma = 0.1$ and $Pr = 1$ with constant $C_{q_w} = 0.1739$ (blue solid line) and variable $C_{q_w} = 0.1328 + 1.235Ra_d^{-0.18}$ (red solid line). Prediction is compared with the Nusselt number data from Iyer *et al.* (2020*a*) averaged at the top/bottom plates Nu (black markers), averaged in the whole volume Nu_v (light-green markers) and the data-fit proposed by them (black dashed line). Data from Samuel *et al.* (2022) (orange markers), scaling proposed by Shraiman & Siggia (1990) (dashed green line), Globe & Dropkin (1959) (dashed pink line) and the estimate from GL theory with updated prefactors from Stevens *et al.* (2013) (dashed brown line) are shown. (*b*) Compensated Nu versus Ra at lower Rayleigh numbers for different Γ (shown in different colours). $Pr = 1$ for $\Gamma = 0.2$ and $Pr = 4.38$ for all other Γ values. Solid lines show current model estimate and dashed lines show the Ahlers *et al.* (2022) model. Markers show data from DNS of Zhang (2019) (open circles) and experiments of Zhang & Xia (2023*b*) (open triangles) at $Pr = 4.38$; and no-tilt case of Zwirner & Shishkina (2018) (filled diamonds) at $Pr = 1$. Dotted lines showing GL theory for each Pr are almost overlapped. For the current model estimates, $C_{q_w} = 0.1328 + 1.235Ra_d^{-0.18}$ is used, and each truncated at a lower limit of $Gr_g = 5\times10^3$.

prediction at higher Ra, although the departure is higher at lower Ra. However, given that the agreement is best captured with the variable C_{q_w}, we choose to use this option further in our analysis. It is evident that the change of regime from 0.3 to 0.5 power law in the tube is responsible for the sharp change in the slope at the critical Rayleigh number.

In figure 3(*b*), we show the results of DNS and experimental studies from Zhang (2019) and Zhang & Xia (2023*b*) for different aspect ratios in the range $0.05 \leqslant \Gamma \leqslant 0.16$ at relatively low Rayleigh numbers and $Pr = 4.38$. Data from the 'non-tilted cases' of Zwirner & Shishkina (2018) at $\Gamma = 0.2$ and $Pr = 1$ are also shown. Zhang & Xia (2023*b*) found delayed onset of convection with decreasing aspect ratio, in line with the predictions of Shishkina (2021) and Ahlers *et al.* (2022). Further to the onset, they observed a steep rise in Nu, followed by an enhanced heat transfer in slender cells compared with the $\Gamma = 1$ (base) case. An estimate using our model for each of the cases is shown in figure 3(*b*), each trimmed at a lower limit for Gr_g at $Gr_{g0} = 5\times10^3$ (see (3.8) and the discussion in § 4.5). That is why the curves corresponding to our model appear to start mid-way in the plot. In particular, the regime of validity of our model starts far from the onset, after the compensated Nu starts to decrease for each case. Ahlers *et al.* (2022) showed that results from various studies with different Γ collapse and lie close to the GL theory estimate, when the Rayleigh number is re-scaled as $Ra_\ell = Ra(1 + 1.49\Gamma^{-2})^{-3/2}$. The modified GL theory estimate for each Γ, based on

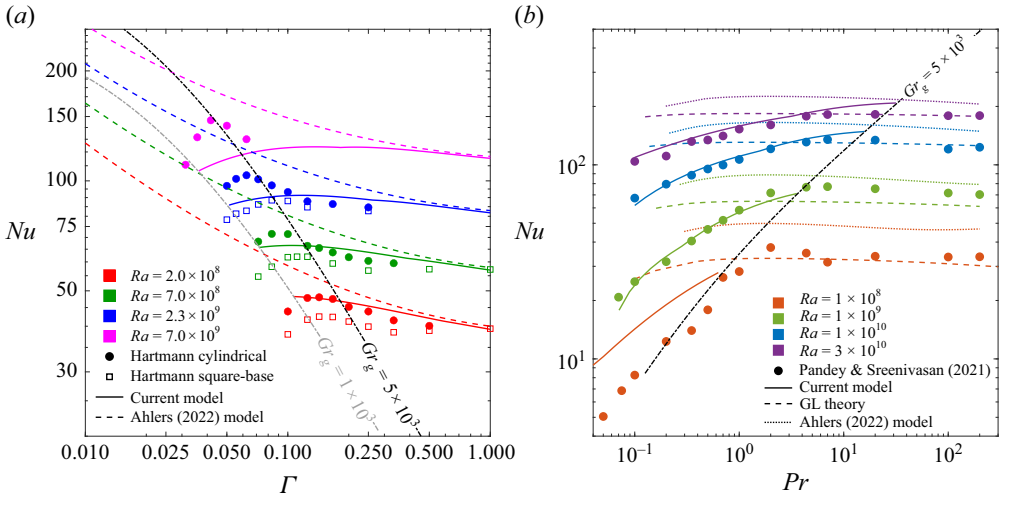

Figure 4. (*a*) Plots of Nu versus Γ for slender RBC using the current model at $Pr = 4.38$ for different Ra, compared with data for cylindrical domain (circular markers) and square-base domain (open square markers) from Hartmann *et al.* (2021). Here $C_{q_w} = 0.1328 + 1.235 Ra_d^{-0.18}$ was used for current model. The prediction by the Ahlers *et al.* (2022) model is shown with dashed lines. Dot-dashed lines show iso-lines of $Gr_g = 1\times10^3$ (grey) and $Gr_g = 5\times10^3$ (black), the lower limit of the current model applicability. (*b*) Plots of Nu versus Pr for four different values of Ra at $\Gamma = 0.1$ compared with the DNS data of Pandey & Sreenivasan (2021) (circular markers). Solid lines show current model estimate, dashed lines show GL estimate ($\Gamma = 1$) and dotted lines show the Ahlers *et al.* (2022) model estimate at the same Ra values. Current model is trimmed at a lower bound of $Gr_g = 5\times10^3$ shown by black dot-dashed curve. The value of C_{q_w} for each case was obtained from GL theory at corresponding Ra_d and Pr (see discussion).

this re-scaling, is shown as the Ahlers model in figure 3(*b*), along with the actual GL theory (Stevens *et al.* 2013) estimate for $\Gamma = 1$. It is worth mentioning that there are no other models that account for the Γ dependence of Nu at such low aspect ratios. It can be seen that within its regime of applicability, our model follows the data from various aspect ratios closely, and that they lie closer to the data than the predictions of the Ahlers model.

Figure 4(*a*) shows the variation of Nu as a function of aspect ratio for different Rayleigh numbers at $Pr = 4.38$ from the DNS studies of Hartmann *et al.* (2021). Data with both cylindrical and square-base domains are shown. The authors reported enhanced heat transfer for small-aspect-ratio cells, and found that there was an optimal aspect ratio Γ_{opt} that maximised the Nusselt number. The Nu augmentation and Γ_{opt} were found to be a function of Rayleigh number and the shape of the container, as can be seen in the figure. Also shown are the Nu predictions of the Ahlers *et al.* (2022) model and the current model for each Ra. Current model is extended to a lower limit of $Gr_g = 1\times10^3$, although we do not know if the 0.3 scaling regime in the tube part is applicable below $Gr_g = 5\times10^3$. Iso-lines of both these Gr_g limits are also shown. We have also extended the model for aspect ratios to $\Gamma = 1$, as the tube resistance becomes negligible and the flux will be controlled entirely by the wall convection. It can be observed that the current model prediction is very close to that of the data even beyond its regime of applicability. In fact, our estimates lie somewhere in between the data for cylindrical and square-base domains. The model predicts a mild maximum for Nu and that this Γ_{opt} is a function of Ra, though the value of this Γ_{opt} is different from that found by Hartmann *et al.* (2021) and the reason is also likely to be different. The model predictions are close to the data

in the range where it is applicable, $Gr_g > 5\times10^3$, and reasonably close even beyond the range to $Gr_g = 1\times10^3$. In general, the predictions are better than that of the Ahlers *et al.* (2022) model, which predicts monotonically increasing Nu with decreasing Γ. At higher aspect ratios ($0.2 \leqslant \Gamma \leqslant 1$) the predictions from our model and the Ahlers model converge. As mentioned above, as Γ approaches unity, the relative contribution of the tube part approaches 0, and the overall model prediction is still accurate.

In figure 4(*b*), the variation of Nu with Pr at different Rayleigh numbers is shown for an aspect ratio of $\Gamma = 0.1$ from the simulations of Pandey & Sreenivasan (2021). The authors report that for $Pr \geqslant 1$ and high Ra, the heat transfer in slender cells is very similar to that in regular cells with $\Gamma \sim 1$. At lower Pr, they found that Nu values in slender cells are much lower than those in wider cells, with steep variation of Nu with Pr especially for the low-Ra cases. The expected behaviour of wide cells ($\Gamma \gtrsim 1$) is shown in the figure by the GL theory for each Ra, along with the modified GL prediction adjusted for Γ dependence using the Ahlers *et al.* (2022) model. The current model estimate for each Ra is also shown, once again trimmed at a lower limit of $Gr_g = 5\times10^3$. The values of C_{q_w} used for the current model were obtained as functions of Pr from curve fits to GL theory at Ra_d values of 10^5, 10^6, 10^7 and 3×10^7 as $0.2616Pr^{0.01238} + 0.03251\times0.9189^{Pr}$, $0.2498Pr^{-0.03176} - 0.01478Pr^{-0.9368}$, $0.2183Pr^{-0.03471} - 0.01787Pr^{-0.7077}$ and $0.2761Pr^{0.05626} - 0.08877Pr^{0.1557}$ corresponding to Ra of 10^8, 10^9, 10^{10} and 3×10^{10}, respectively (although a Pr-independent $C_{q_w} = 0.1328 + 1.235Ra_d^{-0.18}$ also gives reasonable estimates). It can be seen that our model follows the data points remarkably well, except for the lowest Ra of 10^8. In particular, the steep change in Nu at low Pr values is also well captured. This behaviour is due to the strong Pr dependence in the Nu correlations for the tube part. In regular RBC, the Prandtl number effect for Nu scaling is not significant (low or negligible values of exponent p in the usual power-law form $Nu = CRa^nPr^p$), as can be seen by the flat profiles of GL curves. However, in TC, the Pr dependency is very strong, in both the 0.3 and 0.5 regimes (see (3.8)). Thus, in slender RBC, especially at low Ra and Pr values, the tube part plays a dominant role. It should be noted that the TC scaling we adapted from Pawar & Arakeri (2016) has used data that existed in TC only for $Pr \geqslant 1$; however, we see that the capability of the model well surpasses its expected applicability regime (§ 4.5), even giving accurate estimates for Pr as low as 0.1.

4.3. *Temperature drop in the tube part*

One of the main objectives of this paper is to uniquely determine the non-dimensional temperature gradient $\mathrm{d}\widetilde{T}/\mathrm{d}\tilde{z}$ in the tube part which is also equal to the ratio of temperature drop in the tube to the total temperature difference $\Delta T_{tub}/\Delta T$ (2.4) as a function of the total forcing Ra and the aspect ratio of the cell Γ. For turbulent convection in a regular RBC setup, as mentioned above, the core is isothermal due to the efficient mixing by LSC. For slender RBC, we get a linear temperature profile in the tube part, away from the ends, which adds to the overall thermal resistance. This was indeed one of the assumptions we made to derive the generalised Nu–Ra correlation in the previous section. We can get the value of this linear temperature gradient in the core using our model. Using (3.5) and (3.6) to substitute for Nu and Ra with Nu_g and Ra_g in the generalised Nu–Ra correlation (4.8), we have

$$2C_{q_w}^{-3/4}Nu_g^{3/4}Ra_g^{3/4}\Gamma + C_{tub}^{\frac{-1}{1+a}}Nu_g^{\frac{1}{1+a}}Ra_g^{\frac{1}{1+a}}Pr^{\frac{-b}{1+a}} = Ra_g\left(\frac{\mathrm{d}\widetilde{T}}{\mathrm{d}\tilde{z}}\right)^{-1}. \tag{4.10}$$

Now, using the scaling for TC (3.7) and writing Nu_g in terms of Ra_g and simplifying, we get

$$\frac{\mathrm{d}\widetilde{T}}{\mathrm{d}\tilde{z}} = \left(1 + 2C_{q_w}^{-3/4} C_{tub}^{3/4} Ra_g^{\frac{3a-1}{4}} Pr^{\frac{3b}{4}} \Gamma\right)^{-1}. \tag{4.11}$$

This relation gives $\mathrm{d}\widetilde{T}/\mathrm{d}\tilde{z}$ at a particular Ra_g. To rewrite this equation in terms of Ra, we use (3.5):

$$2C_{q_w}^{-3/4} C_{tub}^{3/4} Ra^{\frac{3a-1}{4}} Pr^{\frac{3b}{4}} \Gamma^{3a} \left(\frac{\mathrm{d}\widetilde{T}}{\mathrm{d}\tilde{z}}\right)^{\frac{3(1+a)}{4}} + \frac{\mathrm{d}\widetilde{T}}{\mathrm{d}\tilde{z}} = 1. \tag{4.12}$$

Similar to the generalised Nu–Ra correlation, we have an implicit relation for the non-dimensionalised temperature gradient in the tube part in terms of Ra, Pr and Γ. The values of a and b depend on whether the convection in the tube belongs to the 0.5 (ultimate) or 0.3 (viscous turbulent) regime. For the two regimes of TC, the above relation becomes

$$2C_{q_w}^{-3/4} C_{0.3}^{3/4} Ra^{-1/40} Pr^{21/40} \Gamma^{9/10} \left(\frac{\mathrm{d}\widetilde{T}}{\mathrm{d}\tilde{z}}\right)^{39/40} + \frac{\mathrm{d}\widetilde{T}}{\mathrm{d}\tilde{z}} = 1 \quad \text{for } Gr_{g0} < Gr_g < Gr_{gc}, \tag{4.13a}$$

$$2C_{q_w}^{-3/4} C_{0.5}^{3/4} Ra^{1/8} Pr^{3/8} \Gamma^{3/2} \left(\frac{\mathrm{d}\widetilde{T}}{\mathrm{d}\tilde{z}}\right)^{9/8} + \frac{\mathrm{d}\widetilde{T}}{\mathrm{d}\tilde{z}} = 1 \quad \text{for } Gr_g > Gr_{gc}. \tag{4.13b}$$

The variation of non-dimensional temperature gradient for a slender RBC cell of $\Gamma = 0.1$ and $Pr = 1$ estimated using the current model (4.13*a*,*b*) is shown in figure 5(*a*) for the two different choices of C_{q_w}. The data from Iyer *et al.* (2020*a*) for the same parameter set are also shown for comparison. It can be seen that while the model with variable C_{q_w} approximations shows excellent match with the data, even the constant C_{q_w} approximation gives very reasonable estimates, especially at high Rayleigh numbers. Below the critical Rayleigh number for regime change in the tube part, (4.13*a*) is used, while for above (4.13*b*) is used. The change in regime can be seen as a sudden change in the slope at the critical Rayleigh numbers corresponding to both the C_{q_w} choices. It is also evident that in the 0.5 regime, $\mathrm{d}\widetilde{T}/\mathrm{d}\tilde{z}$ decreases more rapidly compared with that in the 0.3 regime, with increasing Ra. Since $\mathrm{d}\widetilde{T}/\mathrm{d}\tilde{z}$ is also the fraction of the total temperature in the tube, it can be seen that for the current configuration ($\Gamma = 0.1$ and $Pr = 1$), around 10% to 30 % of the temperature drop is in the tube, depending on Ra. The temperature drop in the tube part becomes smaller with increasing Ra, suggesting lower thermal resistance values in the tube part compared with the wall part. As we show in § 4.6, the fraction of temperature drop in the tube depends strongly on aspect ratio and Pr. For $Pr = 1$, $\Gamma = 0.01$, the ratio can be as much as 80 %, and for high Pr it becomes negligible.

In figure 5(*b*), we show the variation of $\mathrm{d}\widetilde{T}/\mathrm{d}\tilde{z}$ with Prandtl number for two different Rayleigh numbers, $Ra = 10^8$ and 10^{10}, for an aspect ratio $\Gamma = 0.1$ predicted using the current model with a lower limit of $Gr_g = 5 \times 10^3$. The data from the simulations of Pandey & Sreenivasan (2021) are shown for comparison. Again, it is seen that the model predicts the variation of temperature gradient in the tube quite well, even for Prandtl number as low as 10^{-2}, showing the beyond-the-expected capability of the model. As shown by Pandey & Sreenivasan (2021), the temperature gradient and hence the relative temperature drop in the tube part is as high as 1 at low Prandtl numbers, and reduces to very low values with increasing Pr. As discussed above, the strong Prandtl number dependence of scaling in TC results in this behaviour. It is worth mentioning that to the best of our

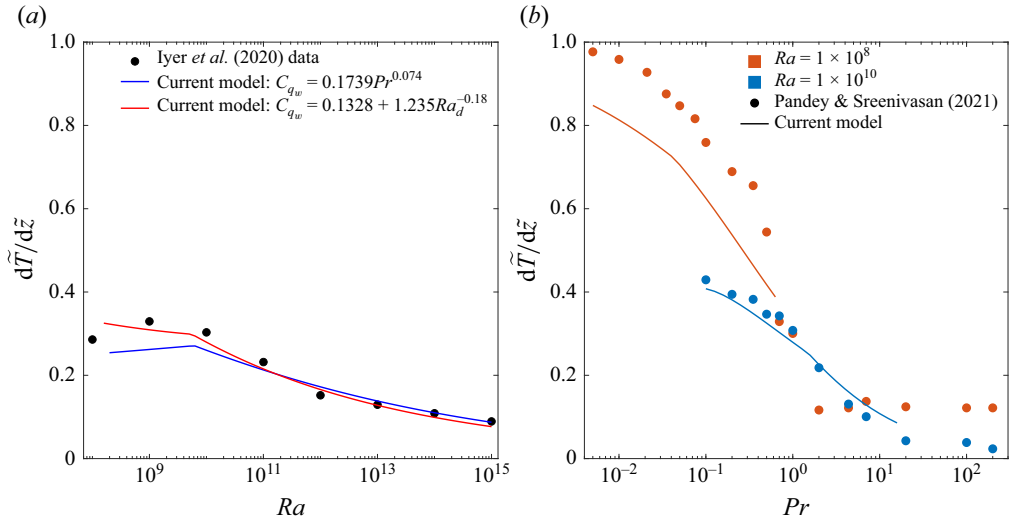

Figure 5. (*a*) Non-dimensional temperature gradient $\mathrm{d}\widetilde{T}/\mathrm{d}\tilde{z}$ (equal to the relative temperature drop in the tube $\Delta T_{tub}/\Delta T$) in the tube part of slender RBC versus Ra for $\Gamma = 0.1$ and $Pr = 1$ calculated using the current model (4.13), compared with Iyer *et al.* (2020*a*) data (black circular markers). Estimates using both a constant $C_{q_w} = 0.1739$ (blue solid line) and variable $C_{q_w} = 0.1328 + 1.235Ra_d^{-0.18}$ (red solid line) are shown. The regime changes from 0.3 to 0.5 power scaling at the critical Rayleigh number $Ra_c \approx 5.3 \times 10^9$ with a sharp change in slope. (*b*) Plot of $\mathrm{d}\widetilde{T}/\mathrm{d}\tilde{z}$ as a function of Pr using the current model (solid lines) at two different Ra values for $\Gamma = 0.1$, compared with the simulation results of Pandey & Sreenivasan (2021) (circular markers).

knowledge, there are no correlations in the literature that predict the temperature gradient or drop in the core for slender RBC, and hence for the figures discussed above, we do not have any correlations or data to compare with; except the DNS data from Iyer *et al.* (2020*a*) and Pandey & Sreenivasan (2021).

An alternative expression for the non-dimensional temperature gradient in the tube can be obtained if the value of Nu is known *a priori*, say from experiments. For this, we note that the ratio of temperature drop in the tube to the total temperature difference is the same as the ratio between the second term of the left-hand side and the right-hand-side term of the generalised $Nu-Ra$ correlation (4.8). That is,

$$\frac{\mathrm{d}\widetilde{T}}{\mathrm{d}\tilde{z}} = \frac{\Delta T_{tub}}{\Delta T} = \frac{C_{tub}^{\frac{-1}{1+a}} Nu^{\frac{1}{1+a}} Ra^{\frac{1}{1+a}} Pr^{\frac{-b}{1+a}} \Gamma^{\frac{-4a}{1+a}}}{Ra} = C_{tub}^{\frac{-1}{1+a}} Nu^{\frac{1}{1+a}} Ra^{\frac{-a}{1+a}} Pr^{\frac{-b}{1+a}} \Gamma^{\frac{-4a}{1+a}}. \tag{4.14}$$

For the two regimes of TC scaling, the above relation becomes

$$\frac{\mathrm{d}\widetilde{T}}{\mathrm{d}\tilde{z}} = C_{0.3}^{-10/13} Nu^{10/13} Ra^{-3/13} Pr^{-7/13} \Gamma^{-12/13} \quad \text{for} \quad Gr_{g0} < Gr_g < Gr_{gc}, \tag{4.15a}$$

$$\frac{\mathrm{d}\widetilde{T}}{\mathrm{d}\tilde{z}} = C_{0.5}^{-2/3} Nu^{2/3} Ra^{-1/3} Pr^{-1/3} \Gamma^{-4/3} \quad \text{for} \quad Gr_g > Gr_{gc}. \tag{4.15b}$$

Thus, we have explicit relations for $\mathrm{d}\widetilde{T}/\mathrm{d}\tilde{z}$ which might be useful if the value of Nu is known beforehand.

The entire procedure described in the previous sections to characterise the heat flux and temperature gradient for a slender RBC configuration (i.e. given Ra, Pr and Γ) can be summarised as follows. The first step is to plot the Ra–Γ parameter space for the

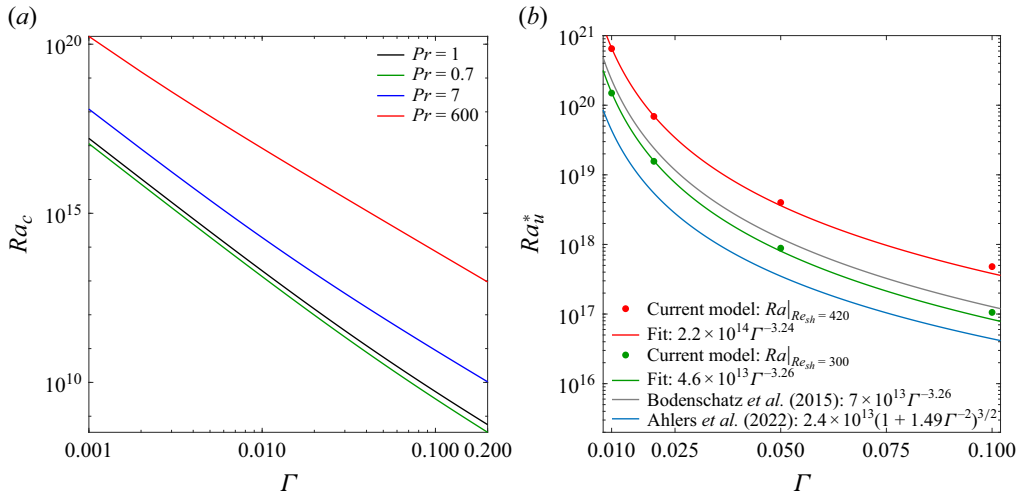

Figure 6. (*a*) Critical Rayleigh number Ra_c of transition between the 0.3 and 0.5 regimes in the tube part, as a function of aspect ratio Γ for different Pr. (*b*) Critical Rayleigh number Ra_u^* of transition to the ultimate regime in the entire cell as a function of aspect ratio Γ for $Pr = 1$ estimated using the current model, such that a critical shear Reynolds number Re_s is achieved. Two estimates with $Re_s = 420$ (red markers) and with $Re_s = 300$ (green markers) are shown. Red and green solid lines are curve fits to these data; grey line is the extrapolation of the estimate by Bodenschatz *et al.* (2015); blue line the estimate by Ahlers *et al.* (2022).

particular Pr, and determine whether the given configuration falls inside the region of applicability (ROA) of the current model (explained in § 4.5). If it does, then the next step is to establish whether it belongs to the 0.3 or the 0.5 regime of TC by finding the critical Rayleigh number $Ra_c = Gr_c Pr$ of transition between the two regimes, corresponding to $Gr_{gc} = 1.6 \times 10^5$ (see Appendix A for details). The next step is to select an expression for C_{q_w} at the particular Pr for wall convection, using any existing scaling relations such as GL theory, as we did in § 3.1. Now, Nu can be estimated by solving (4.9*a*) or (4.9*b*), and $\mathrm{d}\widetilde{T}/\mathrm{d}\tilde{z}$ by solving (4.13*a*) or (4.13*b*), depending on the scaling regime.

4.4. *Critical Rayleigh numbers and transition to ultimate regime*

There are different critical Rayleigh numbers that may be linked to transition between the various convection regimes in slender RBC, and Ra_c is only one among them. The first is the the critical Rayleigh number for onset of convection Ra_{ons}. The aspect ratio dependency of Ra_{ons} is discussed in detail by Shishkina (2021), Ahlers *et al.* (2022) and Zhang & Xia (2023*b*), and we do not discuss this aspect here. Next is Ra_0, marking the transition of convection in the tube part from an (yet) unknown regime to the 0.3 regime, marked by $Gr_g = Gr_{g0}$ (see § 4.5). We do not have enough information about the TC scaling and hence slender RBC scaling below this limit. The next is Ra_c ($= Gr_c Pr$) that we discussed in the previous section, that demarcates the 0.3 (viscous turbulent) and 0.5 (ultimate) regimes in the tube part of the convection. And lastly, Ra_u^*, which gives the value of Ra above which the ultimate regime of convection is obtained in the whole RBC cell, both the tube and wall parts.

The variation of the critical Rayleigh number Ra_c (see Appendix A) with aspect ratio is shown in a log–log plot in figure 6(*a*) for different Prandtl numbers. Only Γ values up to 0.2 are shown since above this limit, the correlations used for the tube part may not be valid. From the figure, it can be seen that the value of Ra_c increases considerably with decreasing aspect ratio for all Prandtl numbers. When the aspect ratio decreases by two

orders of magnitude, the critical Rayleigh number increases by seven orders of magnitude. Thus, for highly slender cells, one cannot expect the 0.5 or the ultimate regime scaling in the tube part until very high Rayleigh numbers, as taller cells lead to lower values of Gr_g for the same Gr ((A4*a*) and (A4*b*)). Variations for four different Prandtl numbers are shown. It can be seen that Ra_c increases considerably with Pr, and high-Pr fluids require extremely high Rayleigh numbers for this transition.

As mentioned above, $Ra > Ra_c$ only implies that the convection in the tube part alone has reached ultimate-regime-type scaling; however, the boundary layer at the walls may not have transitioned to turbulence and the scaling of the global heat flux Nu for the entire cell would not have reached the ultimate regime. Although the existence of such scaling is still debated, it has been proposed that the cross-over to ultimate scaling is achieved when the shear Reynolds number $Re_s = \delta_v u/\nu$ crosses a critical limit of $Re_s \approx 420$ (Grossmann & Lohse 2000, 2002; Ahlers *et al.* 2009), u being the mean wind velocity of the LSC and δ_v the velocity boundary layer thickness (discussed in detail in § 6.4). For slender RBC, we may estimate the critical Rayleigh number for this transition Ra_u^* by finding the Ra at which Re_s crosses the value of 420. For this, we define the shear Reynolds number as $Re_s = \delta_v u_{rms}/\nu$, where, in the absence of LSC, shear is induced on the boundary layer by the fluctuating velocity from the tube part $u_{rms} \sim w_m$. Thus, $Re_s = (\delta_v/d)(u_{rms}d/\nu) = 0.3655 Re_d^{0.5}$ (Re_d is the Reynolds number based on tube width, see § 5), where we used a Blasius-type scaling for the velocity boundary layer $\delta_v/d \sim Re_d^{-0.5}$ and a prefactor of 0.3655 obtained from a curve fit to Iyer *et al.* (2020*a*) data (see § 6.4). For a slender RBC cell with $\Gamma = 0.1$ and $Pr = 1$, we use our model (5.7) and (4.9) and find that the critical Ra for $Re_s = 420$ is $Ra_u^* = 4.8 \times 10^{17}$. For lower aspect ratios, the Ra_u^* estimates are higher, and plotted against Γ in figure 6(*b*). A curve fit to our model prediction gives $Ra_u^* = 2.2 \times 10^{14} \times \Gamma^{-3.24}$. Also shown is an extrapolation of the fit given by Bodenschatz *et al.* (2015), based on their experiments at higher aspect ratios ($\Gamma = 0.33$, 0.5 and 1), and that proposed by Ahlers *et al.* (2022). It can be observed that our exponent $B = -3.24$ in the scaling $Ra_u^* \sim \Gamma^B$ is close to the value of $B = -3.26$ by the former and to the exponent $B = -3$ of Roche (2020) and Ahlers *et al.* (2022) for $\Gamma \ll 1$, based on theoretical arguments. It is interesting that the different approaches give similar aspect ratio dependencies.

It should be noticed, however, that our estimate of Ra_u^* is solely based on the assumption that ultimate regime transition in the entire cell is triggered at $Re_s = 420$. In particular, this approach is valid when the turbulent boundary layer is triggered by the shear of the wind above. The value of 420 is usually used for regular RBC, where the steady wind of LSC is expected to be dominant, even at high Ra. For slender RBC, the time-averaged flow above the boundary layers at high Ra is very weak, as is the case for high-aspect-ratio ($\Gamma = 4$) periodic domains reported recently (Samuel *et al.* 2024). For these cases, the transition to the (potential) ultimate regime could be triggered by a possible destruction of the kinetic boundary layer by turbulent fluctuations (Ahlers *et al.* 2009). If that is the case, the transition could be triggered at even low values of Re_s (based on root mean square (r.m.s.) of fluctuations), since unsteady boundary layers are known to have a lower threshold for transition to turbulence. Hence here we show an estimate of Ra_u^* using $Re_s = 300$ as well, in addition to that of 420. This again gives a very close exponent of $B = -3.26$, although the prefactor has reduced. This estimate lies even closer to the estimates of Bodenschatz *et al.* (2015) and Ahlers *et al.* (2022). It should be reiterated that this approach of finding Ra_u^* based on a critical shear Reynolds number does not guarantee the existence of the ultimate regime beyond this limit, which for slender RBC has not yet been observed. However, this approach gives an estimate of a lower bound for full ultimate transition in slender RBC cells. In summary, both the critical Rayleigh numbers Ra_c for

transition to the ultimate regime in the tube part and Ra_u^* for transition to the ultimate regime of the entire domain are strong functions of aspect ratio, and the more slender the geometry, the higher is the Rayleigh number needed for transition. The above calculation is for $Pr = 1$. It is expected that the value of Ra_u^* will depend on Pr, and may be easily calculated using the same approach.

4.5. *Parameter space*

Next we look at the boundaries of the Ra–Γ–Pr parameter space within which our model is valid. One is the lower limit of applicability of the 0.3 regime in TC, Gr_{g0} (3.8*a*), below which no correlations are available for Nu_g. Based on study reported by Pawar & Arakeri (2016) we arrive at $Gr_{g0} = 5 \times 10^3$, and that is why in figures discussed above, the curves do not span the entire abscissa range, and appear to start mid-way. Secondly, the scaling relations proposed by Pawar & Arakeri (2016) were based on experiments and simulations with $Pr > 1$ only, and so does the expected validity of our correlations. The prefactor C_{tub} and exponents a and b of the general scaling relation for TC (3.7) might have to be modified when studies that encompass a broader range of Gr_g and Pr emerge. A third limitation arises at the wall, where the assumed C_{q_w} scaling is expected to be valid only for Ra_w values greater than around 10^5, i.e. when the wall convection is turbulent and at least one plume or more is present at the wall, i.e. $\lambda_p/d < 1$, where λ_p is the average plume spacing. Plume spacing predicted by the model of Theerthan & Arakeri (1998) and validated by experiments is discussed in detail in § 6.2. At lower Ra_w values, a modified scaling for C_{q_w} needs to be established. And lastly, the domain has to be 'slender' enough for the TC scaling relations to be used. Aspect ratio $\Gamma \leqslant 0.2$ is a reasonable limit so that fully developed, axially homogeneous TC region is present away from the walls. For example, from the vertical profiles of temperature and velocity fluctuations in Zhang & Xia (2023*b*; see their figure 5*b*), axial invariability was observed for $\Gamma \leqslant 0.16$, but not for $\Gamma = 0.3$. This criterion, however, is not very stringent, since the contribution of the tube part in our model diminishes as Γ approaches 1, and the overall scaling controlled by the wall convection approaches that of regular RBC given by the (modified) GL theory, as we discussed earlier (figure 4*a*).

In figures 7(*a*) and 7(*b*), we sketch out the Ra–Γ parameter space for $Pr = 1$ and $Pr = 4.38$, respectively, along with the parameter ranges covered by some of the low-aspect-ratio studies with which we compared our model in the previous sections. The iso-lines of $Gr_{g0} = 5 \times 10^3$; $\Gamma = 0.2$; and $\lambda_p/d = 1$ are shown, which form the expected boundaries within which our model assumptions are valid. This region that we call the ROA of the current model is highlighted using coloured regions. The iso-line of $Gr_{gc} = 1.6 \times 10^5$ splits the ROA into the 0.3 regime (yellow-shaded area) and the 0.5 regime (pink-shaded area) of convection in the tube part. For $Pr = 1$, we have also shown the iso-line for Ra_u^* based on $Re_s = 420$ beyond which the entire cell may transition to the ultimate regime (blue-shaded area in the inset). The lines of Gr_{g0} and $\lambda_p/d = 1$ are very close to each other and have a very similar slope, and depending on Pr, either one of these can be the deciding criterion. While the simulations of Iyer *et al.* (2020*a*) lie deep into the ROA of our model, most of the cases from other studies, Zhang (2019), Hartmann *et al.* (2021), Zhang & Xia (2023*b*) and Zwirner & Shishkina (2018), lie outside or are just inside the boundaries of the ROA; only a few of the points lie inside our ROA. The cases of Pandey & Sreenivasan (2021) are not shown here due to their varying Pr. In the previous sections, we showed that despite the fact that the majority of these studies lie outside the ROA, the model was able to reasonably well predict the *Nu* and temperature gradients for these cases in a wide range of Pr (as low as 0.1) and aspect ratios ($\Gamma \to 1$). Thus, the validity of the model seems to

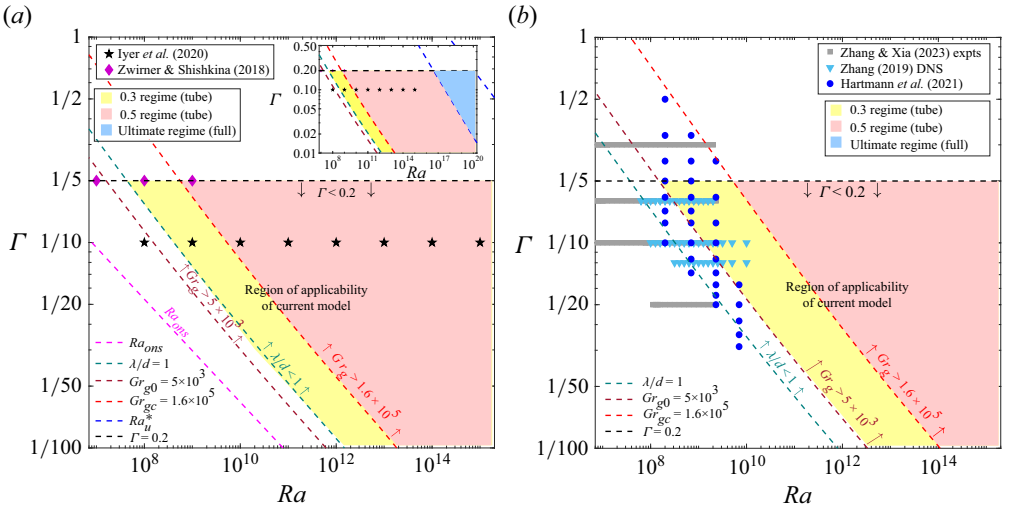

Figure 7. Parameter space of Ra versus Γ for (*a*) $Pr = 1$ and (*b*) $Pr = 4.38$. Dashed lines are iso-lines of Ra_{ons} representing the onset of convection (based on Shishkina (2021)), $Gr_g = Gr_{g0}$, $\Gamma = 0.2$, $\lambda_p/d = 1$, $Gr_g = Gr_{gc}$ and $Ra_u^*|_{Re_s=420}$. Shaded/coloured regions show the expected Region of Applicability (ROA) of the current model. Yellow region: 0.3 (viscous turbulent) regime in the tube part; pink region: 0.5 (ultimate) regime in tube part only; blue region: ultimate regime in the full cell. Inset for (*a*) shows the same figure in an extended range of Γ. Markers indicate the parameter values from the various studies.

extend beyond its ROA. However, Gr_{g0} seems to be a stricter criterion, as below this (yet unknown) value, sharp changes in the kind of TC scalings are expected, evident from the low-Ra data points (near the onset of convection) of Zhang & Xia (2023*b*) in figure 3(*b*). At such low Gr_g values, one may start seeing temperature inversions and locked-flow sublayers as shown in the temperature profiles of Hartmann *et al.* (2021) (see figure 5*e* of their paper and figure S2 in their supplementary material), which depart from the assumed temperature profile of our model (figure 1*c*). It is interesting to note that when a power-law-type scaling is fitted on the $Gr_g = \text{const.}$ lines, i.e. Gr_{g0} and Gr_{gc}, both the corresponding critical Rayleigh numbers Ra_0 and Ra_c have aspect ratio dependencies close to $\Gamma^{-3.8}$ (for $Pr = 1$) and $\Gamma^{-3.6}$ (for $Pr = 4.38$). These exponents are very close to the Γ^{-4} lines given by Zhang & Xia (2023*b*) which demarcate the different regimes in their simulations (see figure 7*c* of their paper). As for the ultimate regime in the entire cell, it can be seen that all the existing studies, including Iyer *et al.* (2020*a*), lie well below the mark needed to cross $Ra_u^* = Ra|_{Re_s=420}$.

4.6. *Effect of aspect ratio and Prandtl number*

In this section, we explore the effect of varying aspect ratio and Prandtl number on the Nusselt number and temperature gradient in the tube part for slender RBC. The compensated plot of Nu with Ra estimated using the current model for different aspect ratios is shown in figure 8(*a*) for $Pr = 1$ using $C_{q_w} = 0.1328 + 1.235Ra_d^{-0.18}$. Here Nu decreases with reducing aspect ratios at all Rayleigh numbers due to the increasing resistance in the tube part resulting in the reduction in overall heat flux. For the Rayleigh number range considered here, there is a reduction of at least 4–5 times in Nu as Γ decreases from 0.1 to 0.01. The change in slope in each curve corresponds to the regime change in the tube part from 0.3 to 0.5. The delayed onset of the 0.5 regime due to the higher critical Rayleigh number is also evident with decreasing aspect ratio. When plotted

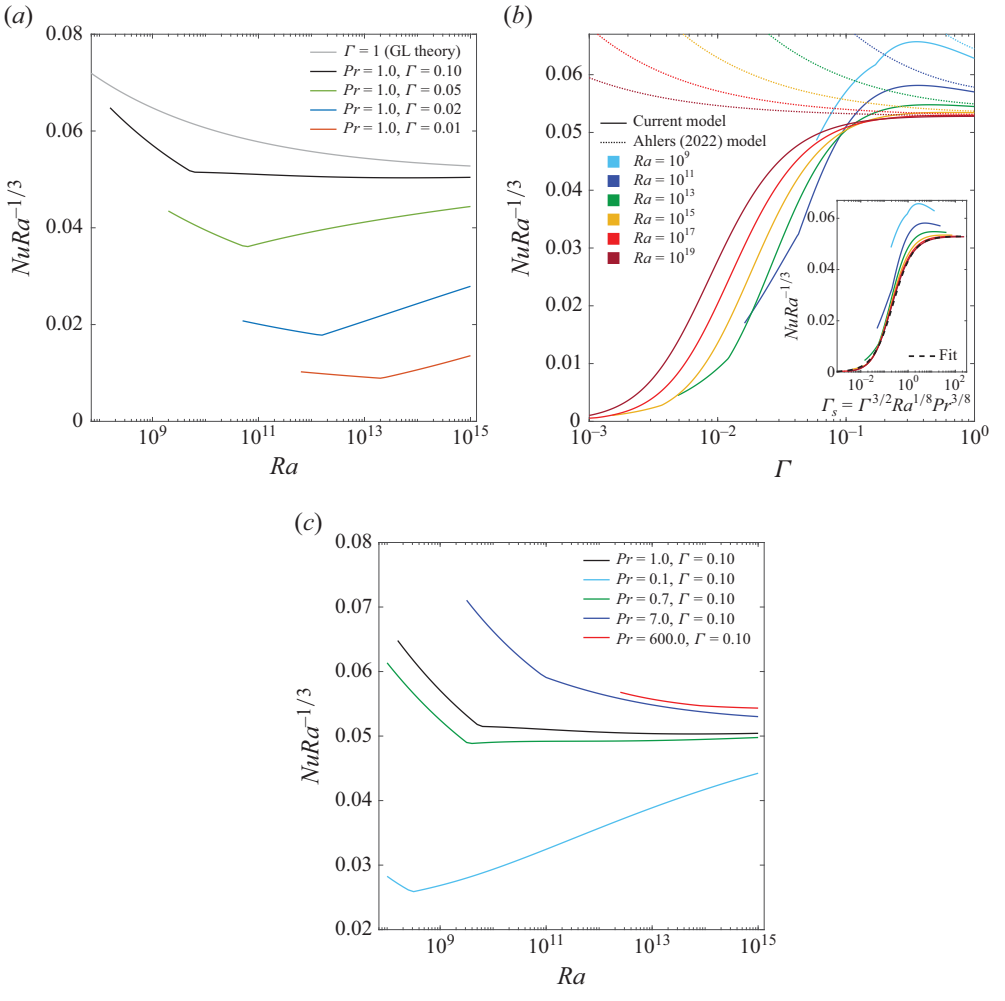

Figure 8. Compensated Nu using the current model (4.9): (a) versus Ra for different aspect ratios (Γ) at $Pr = 1$, (b) versus Γ for different Ra at $Pr = 1$ and (c) versus Ra for different Pr at $\Gamma = 0.1$. In (b), solid lines show current model and dashed lines show the Ahlers *et al.* (2022) model. The inset in (b) shows aspect ratio re-scaled as $\Gamma_s = \Gamma^{3/2} Ra^{1/8} Pr^{3/8}$, and the curves for high Ra collapsing onto a universal curve, given by $0.0265[1 + \tanh(1.18 \log_{10}(\Gamma_s) + 0.75)]$. Each curve is terminated at a lower bound of $Gr_g = 5 \times 10^3$.

against aspect ratio for different Rayleigh numbers (at $Pr = 1$) in figure 8(b), it is clear that there exists an optimum aspect ratio Γ_{opt} at which Nu is maximum, for the lower Rayleigh numbers. This was shown earlier for $Pr = 4.38$ and lower Ra values while comparing the model with the Hartmann *et al.* (2021) results and the associated discussion in figure 4(a). At higher Rayleigh numbers, beyond $Ra \sim 10^{13}$, we do not find the existence of such augmented Nu or optimum aspect ratio: Nu seems to decrease monotonically with reducing Γ. Another interesting observation from figure 8(a,b) is that for $Pr = 1$, above an aspect ratio of $\Gamma = 0.1$, the compensated Nusselt number $NuRa^{-1/3}$ in the 0.5 regime decreases with increasing Ra, while below this limit, it increases with increasing Ra. At $\Gamma = 0.1$, it appears that $NuRa^{-1/3}$ is almost independent of Ra, and is approximately 0.05. At higher Prandtl numbers (not shown here) this observation is consistent, although Γ at which this inversion occurs seems to decrease with Pr.

At lower aspect ratios, the $NuRa^{-1/3}$ curves seem to decline rapidly. At very low aspect ratios ($\Gamma \sim 10^{-3}$), the curves flatten out to exceedingly low values, the value of which depends on Ra. For lower Rayleigh numbers, with reducing Γ, the curves terminate before reaching very small values because of the limit on Gr_g reaching Gr_{g0}, beyond which they cross-over to an unknown regime below the 0.3 regime. The family of these curves for different Ra seem to show similarity to an S-shaped curve. When the aspect ratio Γ is re-scaled as $\Gamma_s = \Gamma^{3/2} Ra^{1/8} Pr^{3/8}$, we find that the curves at different Ra collapse to a single universal curve, especially for higher Rayleigh numbers (inset of figure 8*b*). A least-squares curve fit provides an empirical expression for this universal curve as $NuRa^{-1/3} \approx 0.0265[1 + \tanh(1.18 \log_{10}(\Gamma_s) + 0.75)]$. Although we show the collapse only for $Pr = 1$ here, we have verified that this re-scaling is valid for different Prandtl numbers also ($Pr = 0.1$–600). Note that the expression for the scaled aspect ratio Γ_s is the same as the coefficients in the first term of (4.13*b*), corresponding to the 0.5 regime. That is why the curves start to deviate slightly once they enter the 0.3 regime. We emphasise that the above correlation is valid only for high Rayleigh numbers, particularly for $Ra > 10^{13}$. For lower Ra values, the $NuRa^{-1/3}$ curves start to deviate, as seen in figure 8(*b*).

The (compensated) $Nu-Ra$ plot at different (most commonly encountered) Prandtl numbers for an aspect ratio of $\Gamma = 0.1$ is shown in figure 8(*c*). Note that we have used $C_{q_w} = 0.1328 + 1.235 Ra_d^{-0.18}$ for $Pr = 0.7$, 1 and 7 as the C_{q_w} versus Ra_d curves obtained from the GL theory were very similar for these three cases. For $Pr = 0.1$, we obtained $C_{q_w} = 0.1387 + 14.55 Ra_d^{-0.44}$ and for $Pr = 600$, we obtained $C_{q_w} = 0.1372 + 4.1 Ra_d^{-0.287}$ from curve fits to the respective GL solutions, as discussed in § 3. There is a slight decrease in Nu with decrease in Pr from 600 to 7. As we saw above (figure 4*b* and the associated discussion), Nu decreases steeply with decreasing Pr at low Rayleigh and Prandtl numbers. The effect of Pr on the heat flux mainly comes from the tube part scaling.

The variation of non-dimensional temperature gradient $\mathrm{d}\widetilde{T}/\mathrm{d}\tilde{z}$ (or the fraction of temperature drop $\Delta T_{tub}/\Delta T$) in the tube part with the total Ra for different aspect ratios estimated using (4.13) is shown in figure 9(*a*), for $Pr = 1$. As the aspect ratio Γ decreases, the increased resistance results in a higher relative temperature drop $\Delta T_{tub}/\Delta T$ in the tube part. With a ten-fold decrease in the aspect ratio from 0.1 to 0.01, the relative drop in the tube part increases from about 10%–20 % to around 70 % for the Rayleigh number range considered here. The variation of $\mathrm{d}\widetilde{T}/\mathrm{d}\tilde{z}$ with Γ for different Rayleigh numbers at $Pr = 1$ is shown in figure 9(*b*). The observations are same: relative temperature drop in the tube increases with decreasing Γ, and the variation is pronounced for lower Rayleigh numbers. Note that at $\Gamma = 0.1$, nothing remarkable happens for $\mathrm{d}\widetilde{T}/\mathrm{d}\tilde{z}$, in contrast to the nearly constant behaviour of $NuRa^{-1/3}$ (figure 8*b*). The value of $\mathrm{d}\widetilde{T}/\mathrm{d}\tilde{z}$ increases gradually with reducing aspect ratio until $\Gamma \sim 0.2$, and then increases rapidly with further reduction in Γ for all Ra. At very low aspect ratios, however, the curves tend to flatten out such that the majority of the temperature drop is in the tube part. Once again, when the aspect ratio is re-scaled as $\Gamma_s = \Gamma^{3/2} Ra^{1/8} Pr^{3/8}$, the curves for different Ra collapse onto a single universal curve, even for low Rayleigh numbers (figure 9*b* inset). A curve fit to this universal curve gives $\mathrm{d}\widetilde{T}/\mathrm{d}\tilde{z} \approx 0.5[1 - \tanh(1.09 \log_{10}(\Gamma_s) + 0.88)]$, which is valid for different Prandtl numbers as well (not shown). A close inspection shows departure from the fit when the curves enter the 0.3 regime, although the deviations are extremely small. The collapse is good even at lower Ra, unlike for $NuRa^{-1/3}$. The existence of such universal curves for $\mathrm{d}\widetilde{T}/\mathrm{d}\tilde{z}$ and $NuRa^{-1/3}$ is remarkable, in our opinion. One can very easily get reasonable estimates of the Nusselt number and the temperature gradient, without even solving (4.9) and (4.13), the proposed scaling laws for slender RBC.

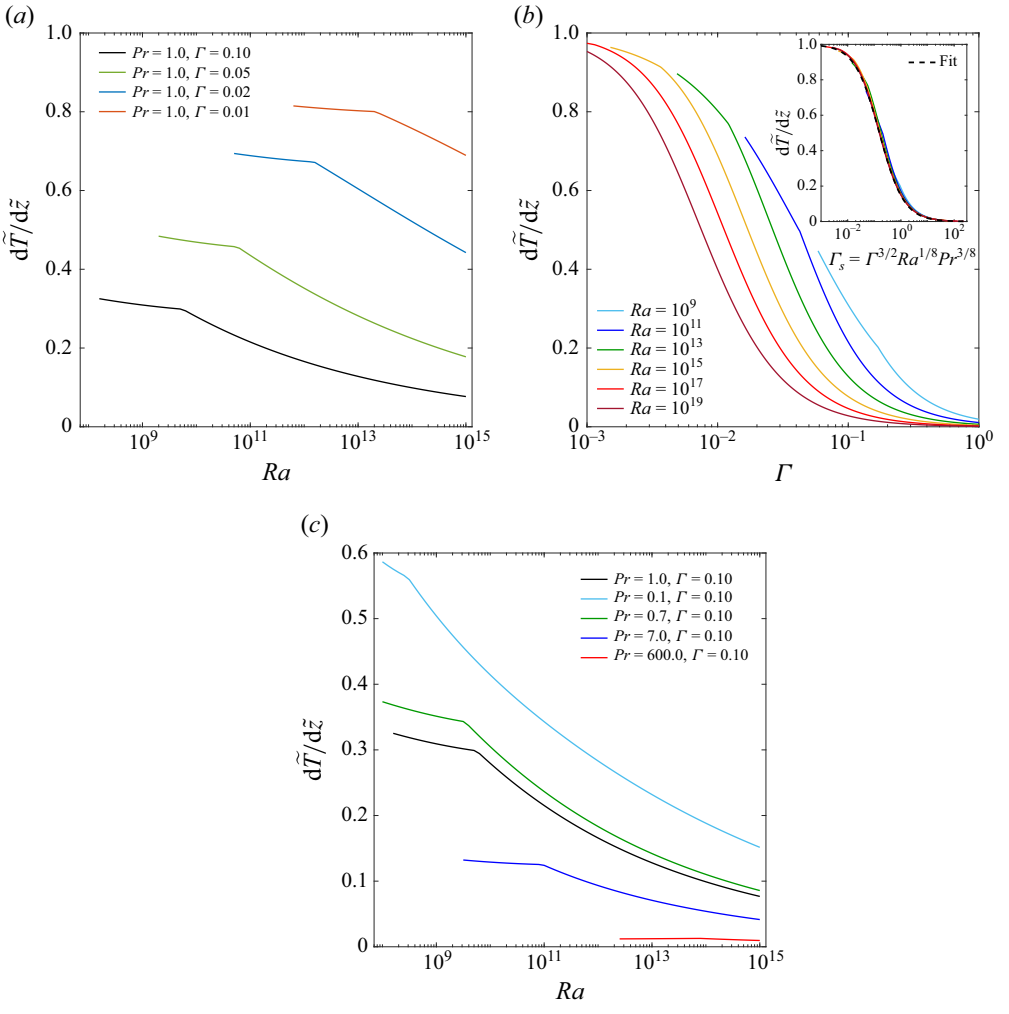

Figure 9. Non-dimensional temperature gradient $\mathrm{d}\widetilde{T}/\mathrm{d}\tilde{z}$ or the fraction of temperature drop in the tube part $\Delta T_{tub}/\Delta T$ using the current model (4.13): (*a*) versus Ra for different aspect ratios (Γ) at $Pr = 1$, (*b*) versus Γ for different Ra at $Pr = 1$ and (*c*) versus Ra for different Pr at $\Gamma = 0.1$. The inset in (*b*) shows that as the aspect ratio is re-scaled as $\Gamma_s = \Gamma^{3/2} Ra^{1/8} Pr^{3/8}$, the curves collapse onto a universal curve given by $0.5[1 - \tanh(1.09 \log_{10}(\Gamma_s) + 0.88)]$.

The variation of $\mathrm{d}\widetilde{T}/\mathrm{d}\tilde{z}$ with Ra for different Prandtl numbers at an aspect ratio of $\Gamma = 0.1$ shows the increasing tube resistance with decrease in Pr (figure 9*c*). At very high Prandtl numbers, the temperature gradient in the tube is negligible, and the core is near isothermal, as in the cases with $\Gamma \gtrsim 1$. This behaviour of $\mathrm{d}\widetilde{T}/\mathrm{d}\tilde{z}$ was already shown when comparing our model with the results of Pandey & Sreenivasan (2021) in § 4.3. We reiterate that C_{q_w} is a very weak function of Pr, meaning that heat transfer in regular RBC is only weakly dependent on Pr for $Pr \gtrsim 1$ and the effect of Pr on Nu in slender RBC is chiefly due to the effect of the tube part, where the Pr dependence is strong. Note that the $Pr = 600$ case has been included in the figures because it corresponds to where the convection experiments are conducted with salt (NaCl) mixed in water to create a density difference. A possible way to do slender RBC experiments with salt is to use permeable

membranes as the top and bottom walls, as was done in Puthenveettil & Arakeri (2005) for studying high-Ra, high-Pr, regular Rayleigh–Bénard-type convection.

5. Scaling of the velocities

For conventional RBC set-ups ($\Gamma \gtrsim 1$), the velocity scale for the LSC at high Rayleigh numbers scales with the velocity of free fall $U_f = \sqrt{g\beta \Delta T H}$, which is the velocity acquired by a parcel of relative density difference from its surroundings, $\Delta\rho/\rho_0 = \beta\Delta T$ rising/falling across a height H under a gravitational field of strength g. The distances are usually non-dimensionalised by the height of the cell H so that dimensionless vertical distance becomes $\tilde{z} = z/H$. Velocities, for example the magnitude of velocity fluctuations $u_{rms} = \langle u_x^2 + u_y^2 + u_z^2 \rangle_{V,t}^{1/2}$ averaged in both space and time, are non-dimensionalised with the free-fall velocity U_f and expressed as $\tilde{u}_{rms} = u_{rms}/U_f$. The Reynolds number $Re = u_{rms}H/\nu$ can then be expressed in terms of the dimensionless velocity as $Re = \tilde{u}_{rms}\sqrt{Ra/Pr}$. For regular RBC set-ups ($\Gamma \gtrsim 1$), the usual scaling of Reynolds number goes as $Re \sim Ra^{1/2}$. For example, Scheel & Schumacher (2017) give the scaling at $Pr = 0.7$, $\Gamma = 1$ as $Re = 0.24Ra^{0.49}$. Iyer *et al.* (2020*a*) give the scaling relation for Reynolds number in the slender RBC setup as $Re = 0.1555Ra^{0.458}$ for $Ra \geqslant 10^{10}$.

For slender RBC cells, however, we use the scaling relations from TC. This argument originates from the idea that the characteristic LSC of regular RBC is not present in slender RBC. Instead, the large-scale flow resemble a helical structure, as reported through iso-surfaces of vertical velocity in Iyer *et al.* (2020*a*). Thus, the flow in the tube part of slender RBC seems more similar to that of TC studies, which we have already established with respect to the scaling of heat flux in the previous sections. For TC at high enough Rayleigh numbers, the scales of temperature and velocity fluctuations proposed by a mixing length model by Arakeri *et al.* (2000) and Cholemari & Arakeri (2009) are

$$T' \sim \left(\frac{\mathrm{d}\overline{T}}{\mathrm{d}z}\right) d = T_m \quad \text{and} \quad w' \sim \sqrt{g\beta \left(\frac{\mathrm{d}\overline{T}}{\mathrm{d}z}\right) d^2} = w_m. \tag{5.1}$$

However, as shown below, the above scaling relations are valid for the 0.5 (ultimate) regime of TC, and need to be modified for the 0.3 (viscous turbulent) regime, i.e. for the data points for the two lowest Rayleigh numbers of the Iyer *et al.* (2020*a*) simulations.

The Reynolds number in TC, $Re_d = u_{rms}d/\nu$ has the tube diameter d as the characteristic length scale. For slender RBC, a similar definition of Re_d for the tube part can be related to the conventional Reynolds number based on total height as $Re_d = Re\Gamma$. For very high Rayleigh numbers, based on the mixing length arguments in (5.1) and backed by experimental observations, Pawar & Arakeri (2016) give the scaling for Reynolds number in TC as

$$Re_d = 0.967 Ra_g^{1/2} Pr^{-1/2} = 0.967 Gr_g^{1/2}. \tag{5.2}$$

Note that we have multiplied by a factor of $\sqrt{3/2}$ the original prefactor of 0.79 given by the authors as they had used the vertical velocity component $u_{z,rms}$ in their definition of Re_d. From the fact that $u_{z,rms}/u_{x,rms} \approx 2$ in TC, we get $u_{rms}/u_{z,rms} \approx \sqrt{3/2}$. It has to be noticed that (5.1) and (5.2) are only valid for the very high (gradient)-Rayleigh-number limit, essentially when the 0.5 regime of flux scaling is applicable (3.8*b*). For the 0.3 power regime (3.8*a*) of flux scaling in TC, no Reynolds-number scaling laws are available yet. Here we propose a scaling relationship for Reynolds number in the 0.3 regime of TC as well.

For obtaining the scales for temperature T_e and velocity fluctuations w_e in the entire turbulent flow regime of TC, Pawar (2015) follows a transfer of energy approach. They argue that as the rate of energy production scales as $\langle \mathscr{P} \rangle \sim g\beta \langle w'T' \rangle$ and the rate of dissipation scales as $\langle \epsilon \rangle \sim w_e^3/d$, a balance between the two gives

$$T_e \sim Nu_g^{2/3} (Ra_g Pr)^{-1/3} \left(\frac{\mathrm{d}\overline{T}}{\mathrm{d}z} \right) d, \tag{5.3a}$$

$$w_e \sim \frac{\alpha}{d} (Ra_g Pr Nu_g)^{1/3}, \tag{5.3b}$$

$$Re_d \sim (Ra_g Nu_g)^{1/3} Pr^{-2/3}. \tag{5.3c}$$

Notice that these scales are general and applicable to both the regimes of turbulent TC. When the flux scaling relation for the 0.5 regime (3.8*b*) is used in (5.3), we recover (5.1) ($T_e = T_m,\ w_e = w_m$) and (5.2) obtained from the mixing length model, which means that they are applicable only in the 0.5 regime. For the 0.3 regime, by substituting the expression for Nu_g from (3.8*a*) to (5.3), we get

$$T' \sim Ra_g^{-2/15} Pr^{2/15} \left(\frac{\mathrm{d}\overline{T}}{\mathrm{d}z} \right) d = Gr_g^{-2/15} T_m, \tag{5.4a}$$

$$w' \sim \frac{\alpha}{d} Ra_g^{13/30} Pr^{17/30} = Gr_g^{-1/15} w_m, \tag{5.4b}$$

$$Re_d \sim Ra_g^{13/30} Pr^{-13/30} = Gr_g^{13/30}, \tag{5.4c}$$

which are the scales of temperature and velocity fluctuations and Reynolds number for the 0.3 regime of TC. Thus, we implicitly assume that similar to the two regimes of flux scaling, there exist two regimes of Reynolds-number scaling, which are separated by the same critical limit $Gr_{gc} = 1.6 \times 10^5$. Matching the scaling laws given by (5.4*c*) and (5.2) at Gr_{gc}, we get a prefactor of 2.15 for Reynolds-number scaling in the 0.3 regime. Thus, the Reynolds-number scaling for the 0.3 regime of TC is given by

$$Re_d = 2.15 Ra_g^{13/30} Pr^{-13/30} = 2.15 Gr_g^{13/30}, \tag{5.5}$$

which is appropriate when $Gr_g < Gr_{gc}$, while (5.2) gives the Reynolds-number scaling for the 0.5 regime in TC when $Gr > Gr_{gc}$. Note that (5.5) and (5.2) are the general relations for Re_d in TC and are not specific to slender RBC. For slender RBC, they can be re-cast in terms of Ra and Γ by using (3.5) as

$$Re_d = 2.15 Ra^{13/30} \left(\frac{\mathrm{d}\widetilde{T}}{\mathrm{d}\tilde{z}} \right)^{13/30} Pr^{-13/30} \Gamma^{52/30} \quad \text{for} \quad Gr_{g0} < Gr < Gr_c, \tag{5.6a}$$

$$Re_d = 0.967 Ra^{1/2} \left(\frac{\mathrm{d}\widetilde{T}}{\mathrm{d}\tilde{z}} \right)^{1/2} Pr^{-1/2} \Gamma^2 \quad \text{for} \quad Gr > Gr_c. \tag{5.6b}$$

Eliminating $\mathrm{d}\widetilde{T}/\mathrm{d}\tilde{z}$ from these equations using (4.15) and noting that $2.15 C_{0.3}^{-1/3} = 0.967 C_{0.5}^{-1/3} = 1.06$, we get a unified relation for Re_d that is applicable for both the regimes as

$$Re_d = 1.06 Ra^{1/3} Nu^{1/3} Pr^{-2/3} \Gamma^{4/3}. \tag{5.7}$$

Although the final relation can be expressed as a single unified expression, the two regimes of Re_d are embedded within the Nu term (which obeys the two regimes of scaling as shown before) on the right-hand side of the above equation.

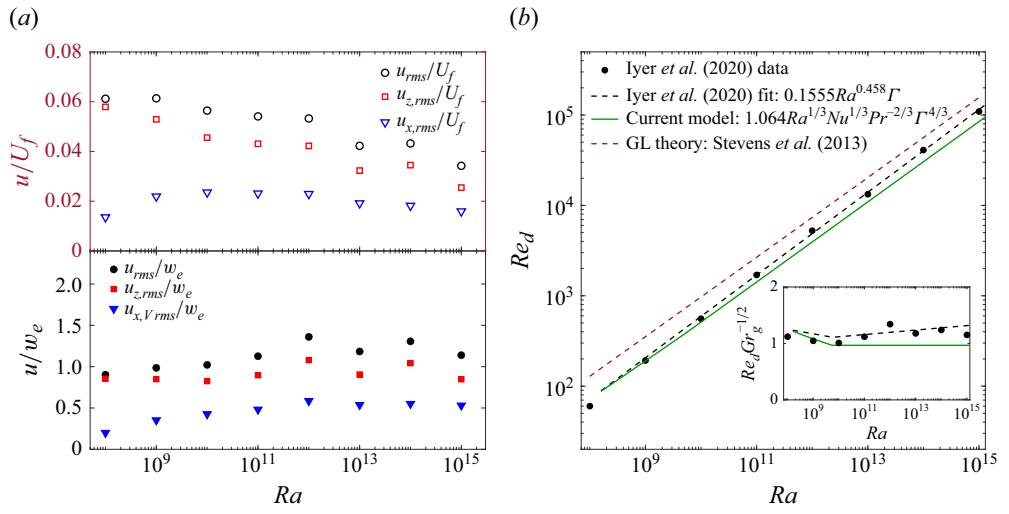

Figure 10. (*a*) The r.m.s. of the velocities in the tube part: $u_{x,rms}$ (horizontal), $u_{z,rms}$ (vertical) and u_{rms} (total) of the data (averaged from $z/H = 0.05$–0.95) from Iyer *et al.* (2020*a*) at different Ra. Open symbols in the top panel: scaled by free-fall velocity U_f; filled symbols in the bottom panel: scaled by TC velocity scale $w_e = 2.15Gr_g^{-1/15}w_m$ for $Ra < Ra_c$ and $w_e = w_m$ for $Ra > Ra_c$. (*b*) Variation of Re_d with Ra for slender RBC using the current model (unified scaling relation (5.7)) for a case of $Pr = 1$, $\Gamma = 0.1$ shown in green solid line. Black circular markers show $Re_d = u_{rms}d/\nu = Re\Gamma$ from the Re data of Iyer *et al.* (2020*a*) and black dashed line shows the fit proposed by them. Dashed brown curve shows the estimate from GL theory (Stevens *et al.* 2013). Inset shows the compensated plot with respect to $Gr_g^{1/2}$.

Figure 10(*a*) shows the r.m.s. velocities for the data of Iyer *et al.* (2020*a*) for different Rayleigh numbers. The data were received through a personal communication with the authors. The r.m.s. of individual components of the velocities, horizontal (lateral) $u_{x,rms}$, vertical (axial) $u_{z,rms}$ and the total magnitude u_{rms}, are shown separately. Here, r.m.s. means $\sqrt{\langle v^2\rangle_{A,t}}$ which is additionally averaged along the height in the tube part $z/H = 0.05$ to 0.95 to exclude the end effects, where v represents any velocity component u_x, u_z or the net magnitude $u = \sqrt{u_x^2 + u_y^2 + u_z^2}$. The velocities are non-dimensionalised by the two different choices of velocity scales. The top part of figure 10(*a*) shows the velocities scaled by the usual choice for RBC, the free-fall velocity U_f based on total height H; and the bottom part of the figure shows the velocities scaled by w_e, a scale from TC perspective. Here, $w_e = 2.15Gr_g^{-1/15}w_m$ for $Ra < Ra_c = 5.3 \times 10^9$ and $w_e = w_m$ for $Ra > Ra_c$. For the first scaling choice U_f, the values of the non-dimensional velocity components in slender RBC are very low ($u_{rms}/U_f \sim 0.06$–0.03) compared with the usual values in regular RBC ($u_{rms}/U_f \sim 0.2$). Also, the values seem decreasing with increasing Ra. When scaled with the TC velocity scale w_e, all the components of velocities approach a constant value (of ~ 1) for the range of Rayleigh numbers considered. The magnitudes of vertical velocity fluctuations are approximately two times those of the horizontal component. These observations are consistent with the experimental observations of Cholemari & Arakeri (2009) and Pawar & Arakeri (2016) in TC studies, where they observed that the fluctuations in the axial component are roughly twice those of the lateral component. Thus, the magnitudes of velocity fluctuations and their anisotropy are very similar in slender RBC to that of TC, confirming the hypothesis that in the tube part the top and bottom end conditions are forgotten away from the ends.

To verify the validity of the Reynolds-number scaling of our model, we compare it with the data from Iyer *et al.* (2020*a*) for the sample case of $\Gamma = 0.1$, $Pr = 1$ in figure 10(*b*). The black circular markers show the data from Iyer *et al.* (2020*a*) (also shown in table 2) and the fit proposed by them is shown with a black dashed curve. The solid green curve shows the prediction using the unified relation (5.7). A compensated plot with respect to $Gr_g^{1/2}$ is also shown in the inset. The prediction from the model is in good agreement with the data. Once again, the change in regime of our prediction is visible as a slight change in the slope at $Ra_c = 5.3 \times 10^9$ although the change in the slope is not as significant as it was for that of the Nu and $\mathrm{d}\widetilde{T}/\mathrm{d}\tilde{z}$ plots. Also, the spread in the Re_d data is due to the spread in the u_{rms} data (figure 10*a*) and we anticipate that longer averaging time could resolve this issue. The estimate from GL theory (Stevens *et al.* 2013), shown as a dashed brown curve, overpredicts the data. This is because for regular RBC, $u_{rms} \sim U_f$ and for slender RBC, $u_{rms} \sim w_m$, underlining the need for separate scaling laws for slender RBC. It is interesting to note that if we use the Nu–Ra fit proposed by Iyer *et al.* (2020*a*), $Nu = 0.055Ra^{1/3}$ in the unified scaling relation (5.7), we get $Re = Re_d\Gamma^{-1} = 0.187Ra^{0.444}$ which is very close to the Re–Ra fit proposed by the authors: $Re = 0.1555Ra^{0.458}$.

Figure 11(*a*,*b*) shows the variation of Reynolds number Re_d for different Rayleigh numbers and aspect ratios for $Pr = 1$ and in figure 11(*c*) for different Pr for $\Gamma = 0.1$ where (5.7) has been used to calculate the Re_d values. Similar to Nusselt number, a significant reduction in Re_d is observed with decreasing aspect ratio. Reynolds number is dependent on the aspect ratio (5.7) as $Re_d \sim \Gamma^{4/3}$ and indirectly through the Nusselt number dependence $Re_d \sim Nu^{1/3}$. The dependency on Prandtl number is more straightforward ($Re_d \sim Pr^{-2/3}$). It can be seen that with increasing Pr, the Reynolds number decreases significantly. For $Pr = 600$, the Reynolds number is a hundredth of its value at $Pr = 1$. Note that for the Reynolds number plots, the change in regime is not very evident in the log–log plots, as the difference in the scaling exponent is very small: $13/30$ versus $1/2$.

6. Near-wall variations

In the previous sections, we discussed the global heat and momentum transport in a slender RBC system. In this section, we discuss the near-wall variations of temperature and the r.m.s. of velocity in a slender RBC cell using the data from the simulations of Iyer *et al.* (2020*a*) received through personal communication. In the following discussion, the term 'walls' refers to the top and bottom horizontal plates. The term 'sidewalls' refers to the vertical (lateral) boundary, which for slender RBC is much larger in area than the top and bottom plates.

For wall-bounded turbulent free convection on horizontal surfaces, two scales exist: the wall (or inner) scales close to the wall where transport of heat and momentum is primarily through diffusion, and the outer (or Deardorff) scales where the LSC is the predominant mode of transport. For a RBC system, the wall scales can be derived using dimensional analysis based on heat flux (Townsend's scales) or based on the temperature difference between wall and the core. For the latter case, Theerthan & Arakeri (1998) give the velocity and length scales as

$$U_w = (g\beta\Delta T_w)^{1/3}(\nu\alpha)^{1/6} \quad \text{and} \quad Z_w = \frac{(\nu\alpha)^{1/2}}{U_w}, \tag{6.1}$$

respectively. These near-wall scales have been successfully used for high-Prandtl-number convection (Puthenveettil & Arakeri 2005) and for studying the near-wall fluctuations of temperature and velocities (Gunasegarane & Puthenveettil 2014). The relationships

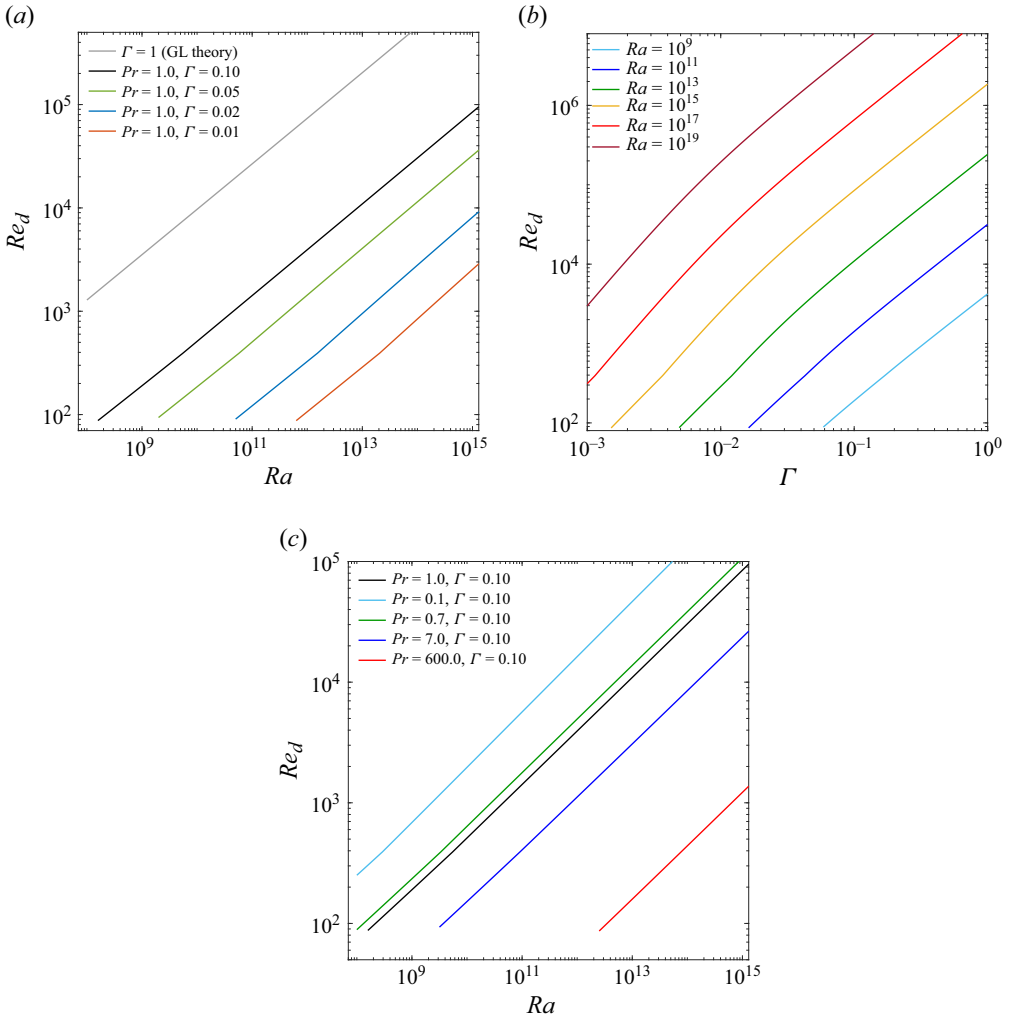

Figure 11. Reynolds number Re_d estimated using the current model (5.7): (*a*) versus Ra for different aspect ratios (Γ) at $Pr = 1$, (*b*) versus Γ for different Ra at $Pr = 1$ and (*c*) versus Ra for different Pr at $\Gamma = 0.1$.

between the different inner scales are given in Theerthan & Arakeri (1998). It is worth mentioning that the ratio of the two inner length scales Z_w and δ_T is exactly equal to the non-dimensional heat flux measure C_{q_w}, from their definitions, i.e.

$$\frac{Z_w}{\delta_T} = C_{q_w} = Ra_{\delta_T}^{-1/3}. \tag{6.2}$$

The outer scales can be derived using dimensional arguments by neglecting the diffusivities. For a RBC system at a prescribed temperature difference ΔT, the outer scales for length and velocity are the separation H and the free-fall velocity $U_f = \sqrt{g\beta\Delta T H}$, or in terms of the heat flux we get the Deardorff scale.

For the slender RBC system, to see the velocity variation near the (top and bottom) walls, one can re-scale the velocity $\tilde{u}$ (which is already non-dimensionalised using U_f)

by using the above wall velocity scale (6.1) as follows:

$$\frac{u_{rms}}{U_w} = \tilde{u}_{rms}\frac{U_f}{U_w} = 2^{1/3}\tilde{u}_{rms}Ra^{1/6}\left(1 - \frac{\mathrm{d}\widetilde{T}}{\mathrm{d}\tilde{z}}\right)^{-1/3}, \tag{6.3}$$

where we used (2.5). Similarly, length scale can be re-scaled using the wall length scale as

$$\frac{z}{Z_w} = \tilde{z}\frac{H}{Z_w} = 2^{-1/3}\tilde{z}Ra^{1/3}\left(1 - \frac{\mathrm{d}\widetilde{T}}{\mathrm{d}\tilde{z}}\right)^{1/3}. \tag{6.4}$$

We can also choose to re-scale the length using thermal boundary layer thickness δ_T. For this, we use (3.1) and get

$$\frac{z}{\delta_T} = 2\tilde{z}\left(1 - \frac{\mathrm{d}\widetilde{T}}{\mathrm{d}\tilde{z}}\right)^{-1} Nu. \tag{6.5}$$

As we have seen in the previous section, the velocities in the tube part scale well with the TC velocity scale w_e, and it would be meaningful to see if this scaling is valid near the walls. In slender RBC, the single outer scale circulation is absent, and instead we have the eddies in the tube, scaling with the diameter and interacting with wall convection. Thus the relevant outer velocity scale is w_e and not U_f. We can simplify things by using the mixing length velocity w_m for scaling throughout the Rayleigh-number range of Iyer *et al.* (2020*a*), since below Ra_c, $w_e = 2.15Gr_g^{-1/15}w_m \approx w_m$, a very weak function of Gr_g, and above Ra_c, $w_e = w_m$. This velocity scale is related to the free-fall velocity U_f as $w_m = U_f(\mathrm{d}\widetilde{T}/\mathrm{d}\tilde{z})^{1/2}\Gamma$. Hence, velocities re-scaled by the mixing length velocity in the tube would be

$$\frac{u_{rms}}{w_m} = \tilde{u}_{rms}\frac{U_f}{w_m} = \tilde{u}_{rms}\left(\frac{\mathrm{d}\widetilde{T}}{\mathrm{d}\tilde{z}}\right)^{-1/2}\Gamma^{-1}. \tag{6.6}$$

Note that although we use w_m as the velocity scale in the following sections, ideally w_e should be used which incorporates the velocity scale change with the regime change. However, for our analysis, w_m is used which gives sufficiently accurate results, while keeping our analysis simple.

6.1. *Temperature variation at the walls*

For slender RBC, thermal boundary layer thickness based on the slope method corresponds to the intersection point between the slope of mean temperature at the wall and the linear temperature in the tube, giving (3.1). For detailed information on this and other methods of defining thermal boundary layer thickness, the reader is referred to Scheel, Kim & White (2012) and the discussion in Ahlers *et al.* (2009). The near-wall variation of the non-dimensional mean temperature $-(\overline{T}(z) - T_0)/\Delta T_w$ along the vertical direction for different Ra of Iyer *et al.* (2020*a*) is plotted in figure 12. Here, $\overline{T}(z) = \langle T\rangle_{A,t}$, with $T_0 = T(z = 0)$. The vertical distance is non-dimensionalised by the boundary layer thickness δ_T using (6.5) in figure 12(*a*) and by the wall scale Z_w using (6.4) in figure 12(*b*). It can be seen that in both the figures, the plots collapse well for different Rayleigh numbers. It can also be noticed that the wall length scale Z_w is also a valid scale near the wall, and most of the variation in mean temperature happens within $Z_w \leqslant 15$, an observation consistent with the literature on conventional RBC (see Theerthan & Arakeri 1998).

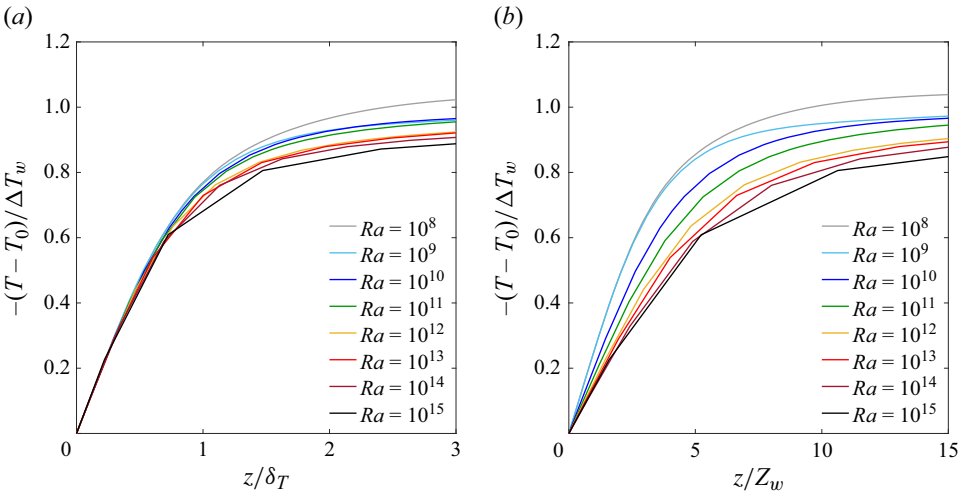

Figure 12. Near-wall profiles of mean temperature of Iyer *et al.* (2020*a*) data along the vertical direction. Temperature is non-dimensionalised by ΔT_w and z non-dimensionalised by (*a*) δ_T and (*b*) Z_w.

6.2. *Plume spacing*

Plumes are the near-wall coherent structures that primarily transport heat from the conduction to the convection layer (Theerthan & Arakeri 1998; Chilla & Schumacher 2012). Very close to the wall, they appear as sheets and further away they may form into mushroom-type structures. They originate as fragments of the thermal boundary layer which detach due to boundary layer instability and move into the bulk followed by broadening due to diffusion and mixing. Higher Rayleigh numbers increase the number of these plumes. The LSC itself is driven partly by merging of groups of localised plumes (Ahlers *et al.* 2009). However, the large-scale wind affects the plume motion also, often aligning them at high enough Ra, as can be seen from the planform views. Based on free-convection experiments on RBC and heated horizontal surfaces, Theerthan & Arakeri (1998) observed the dominant near-wall structures to be a network of randomly spaced and oriented line plumes that are moving about continuously on the surface. The authors proposed a model in which these plumes are fed locally by laminar or viscous free-convection boundary layers either side of each plume. Based on stability arguments they obtained the average spacing of the plumes to be given by $Ra_{\lambda_p}^{1/3} = \lambda_p/Z_w = 52Pr^{-0.012}$, where $Ra_{\lambda_p} = g\beta\Delta T_w\lambda_p^3/(\nu\alpha)$ is the Rayleigh number based on average plume spacing λ_p and Z_w is the wall length scale given in (6.1). The model has been extended to high Pr, $Ra_{\lambda_p}^{1/3} \approx 92$ (Puthenveettil & Arakeri 2005). It has been shown (Theerthan & Arakeri 2000; Puthenveettil & Arakeri 2005; Puthenveettil *et al.* 2011) that the model predictions of plume spacing agree well with what has been obtained in experiments. For slender RBC, at the top and bottom walls, we may express the plume spacing non-dimensionalised with the width of the plate d by invoking the definitions of Ra_{λ_p}, Ra_w and (2.6) as

$$\frac{\lambda_p}{d} = 52Ra_w^{-1/3}Pr^{-0.012} = 65.5Ra^{-1/3}\left(1-\frac{\mathrm{d}\widetilde{T}}{\mathrm{d}\tilde{z}}\right)^{-1/3}\Gamma^{-1}Pr^{-0.012}. \tag{6.7}$$

For the simulation cases of Iyer *et al.* (2020*a*) at $Pr = 1$, the values of Ra_w and plume spacing λ_p/d estimated using (6.7) are given for the various Ra in table 2. The last row,

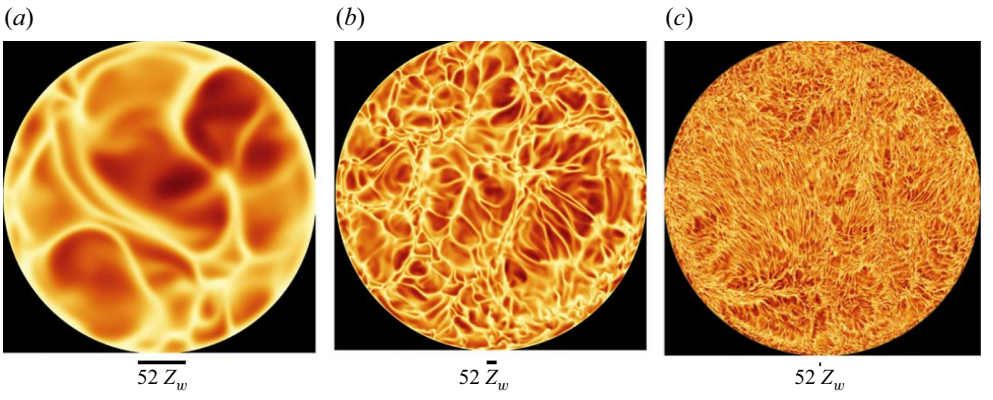

Figure 13. Temperature field at the mid-boundary layer height $\delta_T/2$ showing the plume structure at different Ra: (*a*) $Ra = 10^{11}$; (*b*) $Ra = 10^{13}$; and (*c*) $Ra = 10^{15}$ (reproduced from Iyer *et al.* (2020*a*) with permission). The black horizontal bar below each case shows a scale of $52Z_w$, the expected mean plume spacing. The width of each image corresponds to the tube diameter d.

d/λ_p, gives the approximate mean number of plumes contained within the plate width. With increasing Ra, the plume spacing obviously decreases and a greater number of finer and finer plumes are contained within the plate width. For the lowest-Ra case, notice that $\lambda_p/d > 1$ which means that there is hardly one plume to be expected at any given time. This may be considered as another lower limit for the validity of our model with respect to the convection at the walls, as the value of C_{q_w} might start deviating from our estimate. Thus, from the point of view of the convection at the walls, the applicability of the model is when $\lambda_p/d \lesssim 1$, or equivalently, $Ra_w \gtrsim 10^5$. Contour images of the temperature field near the bottom boundary layer for a few cases from Iyer *et al.* (2020*a*) are reproduced in figure 13. Based on the temperature threshold criteria, these structures can be identified as plumes rising from the bottom surface. An estimate of the mean plume spacing given by $52Z_w/d = 52Ra_w^{-1/3}$ (6.7) is shown below each case for comparison. It can be observed that the structures are, in fact, separated roughly by a magnitude of $\lambda_p \approx 52Z_w$ at least for the high-Ra cases, thus proving the validity of the plume model (6.7) at the walls for slender RBC.

6.3. *Velocity variation at the walls*

As discussed in § 5, in contrast to the LSC of regular-sized RBC, the large-scale structure in slender RBC is of helical nature, which scales with the mixing length velocity w_m of TC. In the tube part, this results in an axially homogeneous turbulence, meaning the statistical quantities are homogeneous along the vertical axis. Near the top and bottom ends of the domain, however, we expect a transition, where this large-scale flow communicates with the near-wall plumes and the (top and bottom) boundary layers. Thus, above the edge of the boundary layer, one should expect velocity fluctuations of the order of the mixing length velocity w_m, and it replaces the LSC velocity scale for RBC with $\Gamma \gtrsim 1$. This is shown in figure 14 where the vertical profiles of the r.m.s. horizontal velocity, $u_{x,rms}$, near the walls are shown for different Ra from Iyer *et al.* (2020*a*) data. The data are averaged in both horizontal plane and time, and the data corresponding to the top and bottom walls have been combined. The velocity is non-dimensionalised using the free-fall velocity U_f in figure 14(*a*) and using the mixing length scale w_m in figures 14(*b*) and 14(*c*).

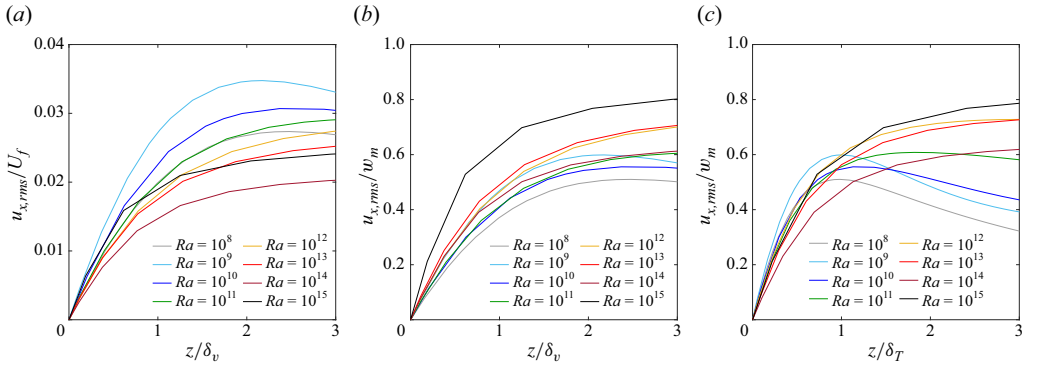

Figure 14. Near-wall profiles of r.m.s. of horizontal velocity fluctuations $u_{x,rms}$ from Iyer *et al.* (2020*a*) data with different choices of non-dimensionalisation for velocity and vertical distance: (*a*) $u_{x,rms}/U_f$ versus z/δ_v, (*b*) $u_{x,rms}/w_m$ versus z/δ_v and (*c*) $u_{x,rms}/w_m$ versus z/δ_T.

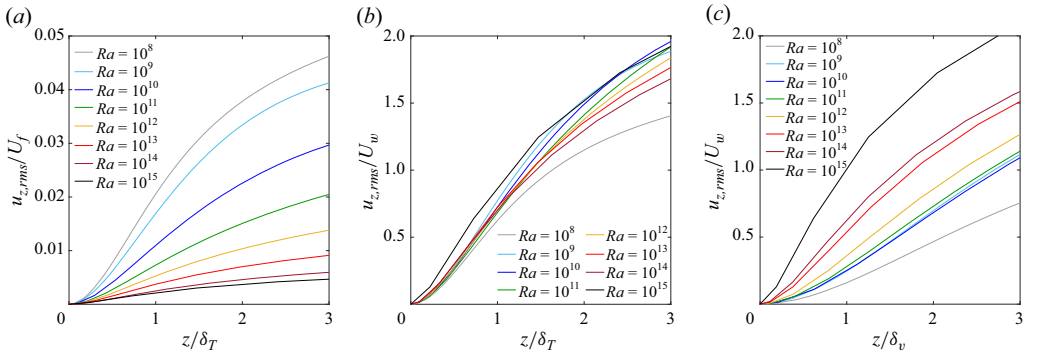

Figure 15. Near-wall profiles of r.m.s. of vertical velocity fluctuations $u_{z,rms}$ from Iyer *et al.* (2020*a*) data with different choices of non-dimensionalisation for velocity and vertical distance: (*a*) $u_{z,rms}/U_f$ versus z/δ_T, (*b*) $u_{z,rms}/U_w$ versus z/δ_T and (*c*) $u_{z,rms}/U_w$ versus z/δ_v.

The vertical distance is non-dimensionalised by the velocity boundary layer thickness δ_v in figures 14(*a*) and 14(*b*) and by the thermal boundary layer thickness δ_T in figure 14(*c*). Here, a Blasius profile is assumed to find the velocity boundary layer thickness (Sun, Cheung & Xia 2008; Ahlers *et al.* 2009) $\delta_v/d = aRe_d^{-1/2}$, $a = 0.3655$. We discuss more about estimating the velocity boundary layer thickness in the next section. It can be seen that scaling the velocities with w_m results in better data collapse and is obviously a better choice for non-dimensionalising the horizontal velocity fluctuations than U_f. It can be also be observed that while scaling with the thermal boundary layer thickness δ_T is not very promising (or with the wall length scale Z_w which is not shown here), scaling with the velocity boundary layer thickness δ_v results in a reasonable collapse of $u_{x,rms}/w_m$ data for different Ra, except for slight deviations at the highest Ra. Thus, it is evident that fluctuations of the horizontal velocity $u_{x,rms}$ grow from 0 at the wall to w_m in the tube part in a distance of around one boundary layer thickness.

However, the r.m.s. of vertical velocity fluctuations, $u_{z,rms}$, show a different behaviour near the walls. The variations of $u_{z,rms}/U_f$ with z/δ_T and $u_{z,rms}/U_w$ with both z/δ_T and z/δ_v for Iyer *et al.* (2020*a*) data are shown in figure 15 for different Ra. While U_f is not a good choice for scaling the vertical component of velocity, a reasonable collapse results

when the wall velocity scale U_w (6.1) is used instead. That U_w is the relevant scale for the vertical velocity is understandable because most of the contribution comes from the plumes. The model proposed by Theerthan & Arakeri (1998) is based on a unit cell of a line plume fed by a boundary layer on either side. It was shown there that in conventional RBC also, data for $u_{z,rms}$ scale well with U_w. It can be noticed that the data collapse better when the distance is scaled with the thermal boundary layer thickness (or the wall length scale Z_w not shown here) than when scaled with velocity boundary layer thickness. This could be due to the fact that vertical velocities scale with the extent of penetration of plumes into the bulk, which again scales with δ_T or Z_w. Thus, we see that while the vertical velocity fluctuations near the wall scale with δ_T or Z_w and U_w, the horizontal velocity fluctuations scale with δ_v and the outer velocity scale w_m, produced by the TC. It is worth mentioning that while moving from the wall to the tube region, the vertical velocity fluctuations grow at a much slower rate than the horizontal components, and the scale reaches the bulk velocity w_m not after one boundary layer thickness, but only around half-a-diameter distance from the wall.

6.4. *Velocity boundary layer*

Similar to the thermal boundary layer, the kinetic or the velocity boundary layer may be defined in many ways. One can define this based on either the mean velocity profile δ_v^M or the (r.m.s. of) the fluctuation velocity profile δ_v^σ. It could be based on local time-averaged profiles or both area- and time-averaged profiles. It could also be based on the components of velocity or the velocity magnitude itself. Again, the boundary layer thickness may be defined to be based on the slope of the vertical profile at the wall δ_v^{sl}, or the distance of the location of the maxima from the wall δ_v^{max}.

The scale of the velocity boundary layer thickness is usually represented as a power law of the form $\delta_v/H \sim Re^\xi$ or $\delta_v/H \sim Ra^\eta$. A simple approximation of $\xi = -1/2$ resulting from laminar boundary layer of Prandtl–Blasius theory has been successful in predicting the mean velocity boundary layer thickness. This approximation was central to the derivation of the GL theory (Grossmann & Lohse 2000, 2004) and is justified due to the low values of shear Reynolds number $Re_s = \delta_v u/\nu$ usually encountered. Above a critical limit of $Re_s \approx 420$, it is believed that the laminar scaling approximations break down and the velocity boundary layers become fully turbulent. Even below this limit when the laminar boundary layer (Blasius) scaling is valid, the mean velocity profile itself departs from the classical Blasius velocity profile due to the continuous chaotic and time-dependent behaviour owing to the continuous detachment of thermal plumes (Ahlers *et al.* 2009). Note that since $Re \sim Ra^{1/2}$, an approximation of $\xi \approx -1/2$ implies that $\eta \approx -1/4$. From numerical simulations of RBC with $\Gamma = 1$ and $Pr = 1$, Verzicco & Camussi (1999) gave a fit $\delta_v^{sl,M}/H = 0.95Ra^{-0.23}$ for the area-averaged boundary layer thickness based on the mean horizontal velocity. Sun *et al.* (2008) performed high-resolution measurements in RBC experiments with water ($Pr = 4.3$) in a rectangular cell of $\Gamma = 1$ in the range $10^9 \leqslant Ra \leqslant 10^{10}$ and proposed $\delta_v/H \sim Ra^{-0.27}$ and $\delta_v/H \sim Re^{-0.50}$ from independently determined Reynolds number, which was consistent with the Prandtl–Blasius scaling. In their case, the boundary layer thickness was estimated from the mean horizontal velocity profiles at the centre of the plate using both the slope and maxima methods, both yielding similar scaling. Numerical simulations of Scheel *et al.* (2012) for $10^5 \leqslant Ra \leqslant 10^9$ and $Pr = 0.4, 0.7$ in a cylindrical cell of $\Gamma = 1$ yield $\delta_v^{sl,M}/H \sim Ra^{-0.18}$ and $\delta_v^{max,\sigma}/H \sim Ra^{-0.25}$, from the mean and r.m.s. horizontal velocity profiles, respectively. Later, owing to the inhomogeneity of the boundary layer dynamics across the area of the plates, Scheel & Schumacher (2014) computed fully local inner and outer scales for

the boundary layer thickness and showed that the conventional boundary layer thickness definition based on the slope method lay in between the averaged values of these scales. For a detailed discussion on various definitions of boundary layer thickness and comparison of numerical and experimental data, we refer the reader to Ahlers *et al.* (2009), Scheel *et al.* (2012) and Scheel & Schumacher (2014).

For slender RBC, as shown in § 6.3, the horizontal velocity near the walls which scales with the mixing length velocity ($u'_x \sim w_m$) acts as the streamwise 'wind' that interacts with the plumes. We also saw that the vertical velocity fluctuations near the walls scale with the wall velocity ($u'_z \sim U_w$). We take the approach that it is the plumes that dictate the growth of the boundary layer, not viscosity (Chandra 2000). We assume that the rate of boundary layer growth along the 'mean flow' direction is proportional to the vertical velocity fluctuations, i.e. $\mathrm{d}\delta/\mathrm{d}t \sim u'_z$, the time derivative being taken in the convective sense. The convective time scale is $\tau = d/w_m$. Thus, $\delta_v(w_m/d) \sim U_w$, or $\delta_v/d \sim U_w/w_m$. Using (6.1) and (5.1), and noticing that $\delta_v/H = (\delta_v/d)\varGamma$, we have

$$\frac{\delta_v}{H} \sim \frac{U_w}{w_m}\varGamma = 2^{-1/3}Ra^{-1/6}\left(1-\frac{\mathrm{d}\widetilde{T}}{\mathrm{d}\tilde{z}}\right)^{1/3}\frac{\mathrm{d}\widetilde{T}}{\mathrm{d}\tilde{z}}^{-1/2}. \tag{6.8}$$

Notice that as the temperature drop in the tube part diminishes, i.e. $\mathrm{d}\widetilde{T}/\mathrm{d}\tilde{z} \to 0$, the above relation implies that $\eta \approx -0.17$. Boundary layer thickness obtained using this relation is compared with Iyer *et al.* (2020*a*) data for slender RBC ($\varGamma = 0.1$) and a few other scaling laws in the literature (for $\varGamma \gtrsim 1$) in figure 16 for various Ra. For extracting the boundary layer thickness from the data, we have used both the methods: based on slope ($\delta_v^{sl,\sigma}$) and based on the location of the maxima ($\delta_v^{max,\sigma}$). Both of these are for the profiles of the r.m.s. horizontal velocity fluctuation, as apparently there is no mean flow or wind in the case of slender RBC. It can be observed that the curve for the boundary layer thickness based on the slope method from the data has a trend very similar to that of the Blasius profile $\delta_v/H = aRe_d^{-1/2}\varGamma$. A curve fit to the data from the slope method gives a prefactor of $a = 0.3655$ for the Blasius scaling. Most of the aforementioned scalings from the literature have a similar trend as they have an η value close to -0.25; however, all of them overpredict the data. It also needs to be mentioned that the correlations cited from the literature correspond to the boundary layer associated with mean flow due to the LSC, which would be present only in the $\varGamma \sim 1$ cells. However, it is evident that the boundary layer thickness based on location of the local maxima, $\delta_v^{max,\sigma}$, has a very different trend, and it follows our prediction (6.8) remarkably well with a prefactor of 0.1313 (obtained from curve fitting). Thus, even though there is no mean flow, the velocity boundary layer thickness estimate using the slope method is well captured by Blasius-like scaling or other predictions in the literature with $\eta \approx -0.25$, whereas the estimate using the maxima method is well captured by the boundary layer thickness determined by the plume-based model (6.8). The reason for the difference in the two scalings is not clear. From the plume structure (figure 13), it is evident that unlike in RBC with $\varGamma \sim 1$, there is no alignment of the plumes in slender RBC suggesting an absence of a persistent large-scale flow. The boundary layer thickness associated with the fluctuating velocity would be due to the fluctuating wind caused by the tube-convection eddies.

6.5. *Velocity variation near the sidewalls*

Although not as important as the top and bottom walls, sidewalls do play an important role in the flow dynamics in RBC, and a predominant one in TC. Ideally, sidewalls are insulated; however, the non-zero conductivities and heat capacities of the sidewalls create additional complexities and the need for sidewall corrections while calculating the

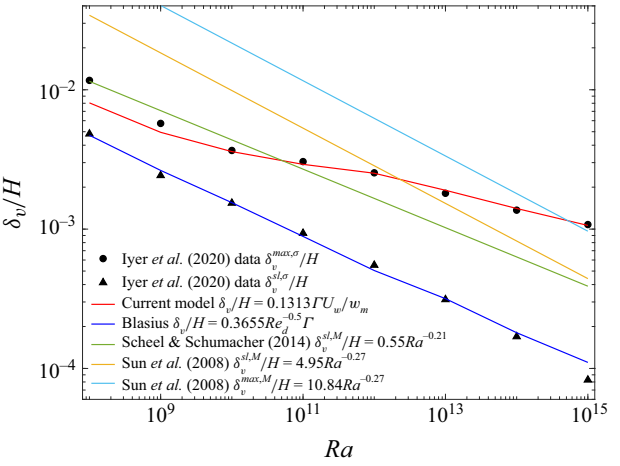

Figure 16. Velocity boundary layer thickness δ_v obtained from the data of Iyer *et al.* (2020*a*) for different Ra. Boundary layer thickness estimates, calculated both using the methods of slope $\delta_v^{sl,\sigma}$ (triangle markers) and maxima $\delta_v^{max,\sigma}$ (circular markers) are shown. Red solid line shows the estimate from the current plume-based model $\delta_v/d \sim U_w/w_m$ (6.8) with an appropriate prefactor of 0.1313. Blue solid line is the Blasius scaling with an appropriate prefactor; other solid lines are various estimates from the literature. The superscripts '*max*' and '*sl* ' stand for the boundary layer thickness definition based on the slope and location of maxima methods, respectively, for the horizontal velocity profile. Similarly, superscripts 'M' and 'σ' stand for boundary layer definition based on the mean and r.m.s., respectively, of the horizontal velocity profile.

convective fluxes in experiments (Roche *et al.* 2001; Verzicco 2002). In fact, performing experiments on slender RBC would be even more challenging, due to large surface area of sidewalls in comparison with the top and bottom walls. For TC and consequently in the tube part of slender RBC, however, the role of the sidewalls is more passive due to the absence of a time-average velocity in the tube at high Ra_g when the flow is turbulent. Away from the sidewalls in the bulk region (towards the centre of the tube), the r.m.s. velocities scale with the mixing length velocity w_m as discussed in § 5. From the radial velocity profile of r.m.s. velocity fluctuations, Cholemari & Arakeri (2009) showed that as the sidewall is approached, the lateral (wall-normal) component starts diminishing early and monotonically to zero at the wall due to kinematic blocking effect. The flow near the wall is akin to shear-free turbulence near a wall, with splat and anti-splat events. Unlike the lateral velocity, the axial (vertical) velocity fluctuation profile peaks near the wall and diminishes rather quickly to zero at the walls due to viscous effects and the no-slip boundary condition. It can be shown that the extent of this viscous affected region may be given by a length scale $l_v \sim \sqrt{\nu\tau}$, where $\tau = d/w_m$ is the eddy turnover time, and can be expressed as $l_v/d \sim Gr_g^{-1/4}$ (Pawar & Arakeri 2016). In figure 17(*a*), the variation in the radial direction of r.m.s. of total velocity fluctuations u_{rms} at the mid-height are shown for Iyer *et al.* (2020*a*) data. Only the near-wall region is shown and the radius r is non-dimensionalised with diameter d of the tube and velocity by the free-fall velocity U_f. At the right end, $r/d = r_0/d = 0.5$, where r_0 is the radius of the tube. The dashed vertical lines show the approximate location of the viscous affected region calculated as $l_v/d = Gr_g^{-1/4}$ from the wall on the right side. It can be seen that most of the variation of the velocity profile is within this length scale for each case. The same data are re-plotted in figure 17(*b*) with the velocity non-dimensionalised with the mixing length velocity w_m and the distance by the viscous length scale l_v, with the coordinate shifted such that left end corresponds to the sidewall. It can be seen that with this choice of scaling for distance

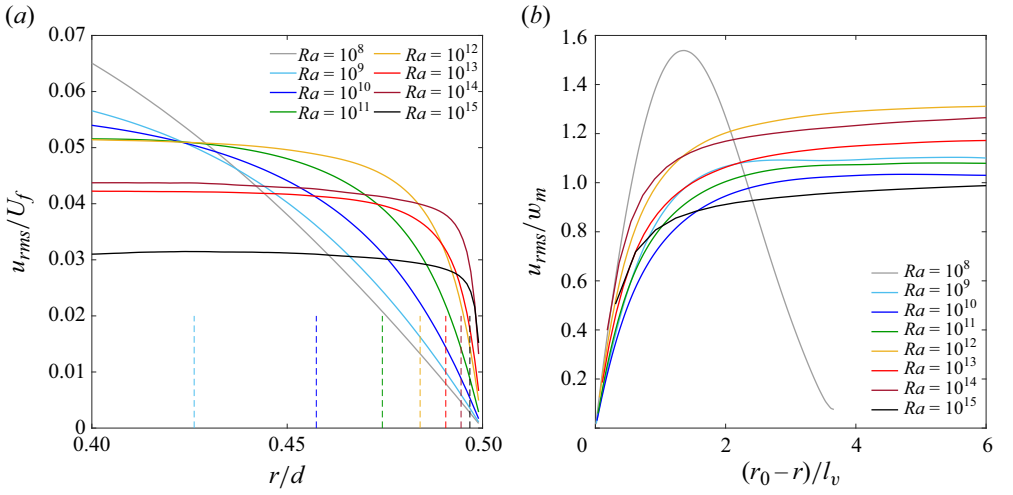

Figure 17. Profiles of r.m.s. of total velocity fluctuations u_{rms} near the sidewall for Iyer *et al.* (2020*a*) data in the radial direction: (*a*) u_{rms}/U_f versus r/d and (*b*) u_{rms}/w_m versus $(r_0 - r)/l_v$. Here, $r_0 = d/2$ is the radius of the tube and $l_v = \sqrt{\nu\tau} = \sqrt{\nu d/w_m}$. Data are sampled at mid-height $z/H = 0.5$ and averaged in the azimuthal direction and time. Dashed vertical lines in (*a*) show the location of l_v measured from the wall (right end) for various Ra.

and velocity, the data for different Ra collapse onto each other within a small error margin, except for the smallest Ra. The viscous affected, boundary layer-like region falls within a distance of $r/l_v \approx 2$ from the sidewall for all the cases. Note that we have used the total velocity fluctuation profile here and not the vertical velocity which would have shown a peak at the edge of the viscous affected region where vertical velocity fluctuations are maximum. The total velocity r.m.s. increases monotonically from 0 at the wall and reaches the mixing length velocity within a few l_v lengths. In fact, the reason for change in the scaling regime from 0.3 to 0.5 in TC can be traced back to the extent of this viscous affected region (Pawar & Arakeri 2016). For the 0.3 scaling regime, the viscous region extends to a significant portion of the tube as in the lowest-Ra case $Ra = 10^8$ in figure 17. Note that for this case, the entire width of the tube is around $3.5l_v$, meaning that the entire tube is affected by viscosity. For the 0.5 regime, the extent of the viscous region is very small and negligible compared with the tube width, meaning the flow in the bulk is unaffected by diffusive effects resulting in the ultimate (1/2-power) scaling.

7. Slender RBC versus TC

It is compelling to compare the flux transport between slender RBC and TC, given that removing the top and bottom plates of the former and replacing them with constant-temperature reservoirs results in the latter. Consider a slender RBC and a TC setup with the same dimensions (d, H and thus Γ) and maintained at same temperature difference $\Delta T = T_h - T_c$ across its ends (and therefore same Ra) as in figures 1(*b*) and 1(*c*) in the limit of sufficiently small aspect ratio ($\Gamma \ll 1$). In TC, due to the absence of the walls at the ends, the fluid at temperatures T_h and T_c can enter and exit freely and thus ideally the linear temperature gradient in the tube ($\mathrm{d}\overline{T}/\mathrm{d}z$) should approach $\Delta T/H$. However, at both the ends where tube joins the reservoirs, there exists the possibility of development regions characterised by nonlinear temperature profiles. Consequently, the temperature gradient

in the tube need not be equal to $\Delta T/H$ and the ratio of the actual temperature gradient to the ideal temperature gradient may be expressed as $(\mathrm{d}\overline{T}/\mathrm{d}z)/(\Delta T/H) = K_{TC}$. Cholemari & Arakeri (2005) give this ratio in a functional form, $K_{TC} = (1 + 2(k_\rho - k_H)\Gamma)^{-1}$. Here, $k_\rho = \Delta\rho_e/(\mathrm{d}\overline{\rho}/\mathrm{d}z)d$ is the ratio of density drop $\Delta\rho_e$ at the tube ends to the density drop over one-diameter distance in the tube region and $k_H = L_e/d$ is the ratio of the length of development region L_e to the tube diameter. Additionally, Cholemari & Arakeri (2005) using curve fitting to data from salt experiments showed that $k_\rho \approx 3.1$ and $k_L \approx 1$, giving $K_{TC} = (1 + 4.2\Gamma)^{-1}$. Now, the ratio of the (absolute) temperature gradients of TC and in the tube part of slender RBC can be written as

$$\frac{\left(\frac{\mathrm{d}\overline{T}}{\mathrm{d}z}\right)_{TC}}{\left(\frac{\mathrm{d}\overline{T}}{\mathrm{d}z}\right)_{SR}} = \frac{K_{TC}\Delta T/H}{\Delta T_{tub}/H} = K_{TC}\frac{\Delta T}{\Delta T_{tub}} = K_{TC}\left(\frac{\mathrm{d}\widetilde{T}}{\mathrm{d}\tilde{z}}\right)_{SR}^{-1}, \tag{7.1}$$

where $(\mathrm{d}\widetilde{T}/\mathrm{d}\tilde{z})_{SR}$ is the non-dimensional temperature gradient in the tube part of slender RBC, which we discussed in detail earlier. In the ongoing discussion, we use subscripts TC and SR to distinguish between TC and slender RBC, respectively. From the definitions, it is easy to show that the ratio of the gradient Rayleigh numbers between TC and slender RBC is

$$\frac{Ra_{g,TC}}{Ra_{g,SR}} = \frac{\left(\frac{\mathrm{d}\overline{T}}{\mathrm{d}z}\right)_{TC}}{\left(\frac{\mathrm{d}\overline{T}}{\mathrm{d}z}\right)_{SR}} = K_{TC}\left(\frac{\mathrm{d}\widetilde{T}}{\mathrm{d}\tilde{z}}\right)_{SR}^{-1}. \tag{7.2}$$

Similarly, the ratio of the gradient Nusselt numbers is

$$\frac{Nu_{g,TC}}{Nu_{g,SR}} = \frac{q''_{TC}}{q''_{SR}}\frac{\left(\frac{\mathrm{d}\overline{T}}{\mathrm{d}z}\right)_{SR}}{\left(\frac{\mathrm{d}\overline{T}}{\mathrm{d}z}\right)_{TC}} = \frac{q''_{TC}}{q''_{SR}}K_{TC}^{-1}\left(\frac{\mathrm{d}\widetilde{T}}{\mathrm{d}\tilde{z}}\right)_{SR}. \tag{7.3}$$

Thus, the ratio of the heat fluxes between TC and slender RBC of same dimensions subjected to the same temperature difference is

$$\frac{q''_{TC}}{q''_{SR}} = \frac{Nu_{g,TC}}{Nu_{g,SR}}K_{TC}\left(\frac{\mathrm{d}\widetilde{T}}{\mathrm{d}\tilde{z}}\right)_{SR}^{-1}. \tag{7.4}$$

In a similar manner, using (5.3*c*), the ratio of Reynolds numbers (or velocity) in TC and slender RBC can be obtained as

$$\frac{Re_{d,TC}}{Re_{d,SR}} = \frac{u_{rms,TC}}{u_{rms,SR}} = \left(\frac{Ra_{g,TC}}{Ra_{g,SR}}\right)^{1/3}\left(\frac{Nu_{g,TC}}{Nu_{g,SR}}\right)^{1/3}. \tag{7.5}$$

To see realistic values, let us assume both TC and slender RBC are in conditions where the scalings fall in the 1/2-power regime, so that $Nu_{g,SR} \sim Ra_{g,SR}^{1/2}$ and $Nu_{g,TC} \sim Ra_{g,TC}^{1/2}$. Thus, $Nu_{g,TC}/Nu_{g,SR} = (Ra_{g,TC}/Ra_{g,SR})^{1/2} = K_{TC}^{1/2}(\mathrm{d}\widetilde{T}/\mathrm{d}\tilde{z})_{SR}^{-1/2}$ which in turn means that

$$\frac{q''_{TC}}{q''_{SR}} = K_{TC}^{3/2}\left(\frac{\mathrm{d}\widetilde{T}}{\mathrm{d}\tilde{z}}\right)_{SR}^{-3/2} \quad \text{and} \quad \frac{Re_{d,TC}}{Re_{d,SR}} = K_{TC}^{1/2}\left(\frac{\mathrm{d}\widetilde{T}}{\mathrm{d}\tilde{z}}\right)_{SR}^{-1/2}. \tag{7.6}$$

For example, for $\Gamma = 0.1$ and $Pr = 1$, $K_{TC} \approx 0.7$, at $Ra = 2 \times 10^{11}$, $(\mathrm{d}\widetilde{T}/\mathrm{d}\tilde{z})_{SR} \approx 0.2$ gives $q''_{TC}/q''_{SR} \approx 6.54$; $Re_{d,TC}/Re_{d,SR} \approx 1.87$ and at $Ra = 10^{14}$, $(\mathrm{d}\widetilde{T}/\mathrm{d}\tilde{z})_{SR} \approx 0.1$ gives

$q''_{TC}/q''_{SR} \approx 18.5$; $Re_{d,TC}/Re_{d,SR} \approx 2.64$. It should be noted that here we used the correction factor $K_{TC} = (1 + 4.2\Gamma)^{-1}$ from Cholemari & Arakeri (2005) which was estimated from high-Pr (salt) experiments. For low-Pr fluids, recent TC experiments (Pawar 2015) show that the temperature drop at the ends is negligible, so that $K_{TC} \approx 1$. If we use this condition, we can see that at $Ra = 2 \times 10^{11}$, $q''_{TC}/q''_{SR} \approx 11.2$; $Re_{d,TC}/Re_{d,SR} \approx 2.24$ and at $Ra = 10^{14}$, $q''_{TC}/q''_{SR} \approx 31.6$; $Re_{d,TC}/Re_{d,SR} \approx 3.16$. Thus, we see that the ratio of the heat flux in TC is at least an order of magnitude higher that that in slender RBC with the same dimensions and forcing, while the velocities are a few times higher.

8. Conclusion

In this paper, we have shown that turbulent convection in slender RBC ($\Gamma < 0.2$) may be considered to consist of two parts: one away from the two horizontal walls, where it is like TC, and one near the horizontal walls, where it is similar to conventional ($\Gamma \gtrsim 1$) RBC, that we term wall convection. The heat flux is determined by the sum of thermal resistances in the two parts. TC and wall convection have different flow features and scaling laws. TC, because of lateral confinement, is characterised by linear temperature and axially homogeneous conditions in the mean (Arakeri *et al.* 2000; Cholemari & Arakeri 2009). Depending on the (gradient) Rayleigh number, at least two regimes exist for the heat flux transport (Pawar & Arakeri 2016). For the wall convection, we showed that it is convenient to use a 'local' non-dimensional heat flux parameter C_{q_w} (Arakeri *et al.* 2024) which is only weakly dependent on Ra, and can be obtained from existing scaling relations for regular-sized RBC or other geometrically similar configurations, such as convection near heated horizontal walls. An advantage with C_{q_w} is that, unlike Nu, it is independent of length scale, and is related to the Rayleigh number based on the thermal boundary layer thickness. Based on the thermal resistance model, we derived generalised scaling laws for the non-dimensional heat flux Nu, mean vertical temperature gradient in the tube part $\mathrm{d}\widetilde{T}/\mathrm{d}\tilde{z}$ and Reynolds number Re_d in terms of Rayleigh number, aspect ratio and Prandtl number. The predictions using this model show excellent agreement with many of the recent studies involving convection in slender geometries (Iyer *et al.* 2020*a*; Pandey & Sreenivasan 2021). Even though in several of the studies (Zwirner & Shishkina 2018; Zhang 2019; Hartmann *et al.* 2021; Zhang & Xia 2023*b*) the parameters fall near the boundaries where our model is applicable, the model predictions compare well with the data. An important feature of slender RBC, well captured by the model, is the strong dependence of Nu on Pr, unlike in regular ($\Gamma \sim 1$) RBC. This Pr dependence arises mainly from the tube part of the convection. We further observed that when plotted against a scaled aspect ratio $\Gamma_s = \Gamma^{3/2} Ra^{1/8} Pr^{3/8}$, the variations of the compensated Nusselt number $NuRa^{-1/3}$ and the fractional temperature drop in the tube part ($\mathrm{d}\widetilde{T}/\mathrm{d}\tilde{z}$) for sufficiently high Rayleigh numbers ($Ra > 10^{13}$) and Prandtl numbers ($Pr > 0.1$) collapse approximately onto two universal S-shaped curves, which are well fitted by hyperbolic tangent functions. These correlations will be useful in estimating these quantities in high-Ra slender RBC.

We showed that the near-wall variations of mean temperature and r.m.s. velocities collapse for different Ra, when scaled appropriately with near-wall length and velocity scales. In addition, we showed that for the data in Iyer *et al.* (2020*a*), the velocity boundary-layer thickness estimated by the slope method follows the Prandtl–Blasius scaling, whereas that based on the location of the horizontal r.m.s. velocity maxima follows the prediction

based on a plume-based model for boundary layer growth. Finally, we compared the flux transport in slender RBC with that of TC, and show that fluxes in the latter are much higher than in the former.

We have seen that for most of the scaling relations for slender RBC, the width/diameter of the domain d is the relevant length scale rather than the vertical separation H. For example, heat flux at the walls C_{q_w} depends on Ra_d; and the flux in the tube Nu_g and the Reynolds number Re_d depend on the gradient Grashof number Gr_g. This is in line with the observations of Shishkina (2021) and Ahlers *et al.* (2022) that for RBC with $\Gamma \ll 1$, the relevant length scale approaches the diameter of the plates $\ell \approx d$. We also saw that the critical Rayleigh number Ra_c (or critical Grashof number Gr_c) that determines the transition between the 0.3 and 0.5 regimes of scaling strongly increases with reducing Γ. For $Ra > Ra_c$, the (0.5) ultimate regime is achieved in the tube part, and for $Ra < Ra_c$, the ultimate regime will not be attained in the tube part, let alone the full domain. Thus, crossing Ra_c will be a necessary condition for attaining the final transition to the possible ultimate scaling in the domain, in addition to the boundary layers at the walls becoming fully turbulent. We also showed that the critical Rayleigh number Ra_u^* of transition of the full domain into the ultimate regime may be estimated by using the criterion of shear Reynolds number at the boundary layers crossing a threshold value of 420, and obtained that $Ra_u^* \sim \Gamma^{-3}$ for slender RBC; for $\Gamma = 0.1$, our predicted value of Ra_u^* is 4.8×10^{17}. These scalings may be used for designing a slender RBC to attain an overall ultimate regime.

We reiterate that in the Ra–Γ–Pr parameter space, the correlations on which the current model is based are valid only when certain conditions are satisfied. The existence of a tube part is assumed which would be reasonable for low aspect ratios ($\Gamma < 0.2$) only. For the near-wall flow, the wall Rayleigh number Ra_w should be such that the at least one or more plumes are present, i.e. $Ra_w \gtrsim 10^5$ or $\lambda_p/d \leqslant 1$. For the tube part, it is required that the gradient Grashof number Gr_g be above a certain, but yet unknown limit Gr_{g0} which is expected to be approximately 5×10^3. Also, the correlations for the TC part that we have used in the model are for moderate to high Prandtl numbers ($Pr \gtrsim 1$). In summary, the regime of validity of the current model is when $Gr_g \geqslant 5 \times 10^3$, $\lambda_p/d < 1$, $Pr \gtrsim 1$ and $\Gamma \leqslant 0.2$, though the model seems to reasonably well predict data for Pr as low as 0.1, and for $\Gamma \to 1$. The approach of our model of considering slender RBC as the sum of two thermal resistances may be extended beyond the current ROA with appropriately modified tube and wall-scaling relations.

Acknowledgements. As the reader might have already noticed, we refer extensively to Iyer *et al.* (2020*a*), which inspired us to commence the study. We are indebted to Professor K.R. Sreenivasan, Professor J. Schumacher and Professor Janet D. Scheel for providing the data from their simulations and for their inputs on the manuscript. We thank the anonymous reviewers whose suggestions significantly improved the manuscript.

Declaration of interests. The authors report no conflict of interest.

Appendix A. Relation between Gr_g and Gr: estimating Gr_c

In the relations for Nu and $\mathrm{d}\widetilde{T}/\mathrm{d}\tilde{z}$ (§ 4), the critical Rayleigh (or Grashof) number of transition between the two scaling regimes of TC is unknown to begin with. What we know is the critical gradient Grashof number $Gr_{gc} = 1.6 \times 10^5$. We need a relation between Gr (based on the total temperature difference ΔT) and Gr_g (based on temperature gradient

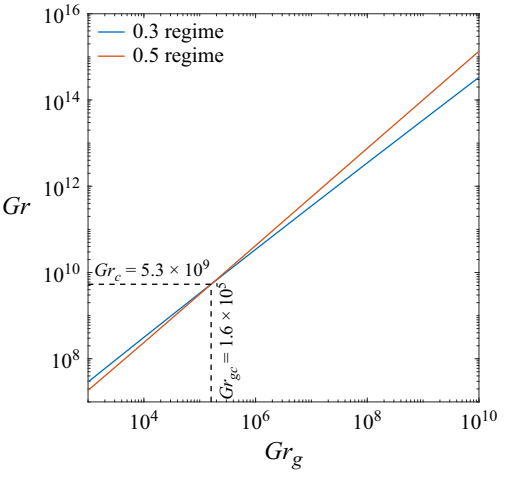

Figure 18. Plots of Gr versus Gr_g for 0.3 and 0.5 power law regimes (A3) for $\Gamma = 0.1$ and $Pr = 1$ with $C_{q_w} = 0.1328 + 1.235 Ra_d^{-0.18}$.

$\mathrm{d}\overline{T}/\mathrm{d}z$ in the tube part) to find the critical Grashof number Gr_c. To do so, we use $\mathrm{d}\widetilde{T}/\mathrm{d}\tilde{z} = (Ra_g/Ra)\Gamma^{-4}$ from (3.5) to eliminate $\mathrm{d}\widetilde{T}/\mathrm{d}\tilde{z}$ in (4.12), so that

$$2C_{q_w}^{-3/4} C_{tub}^{3/4} Ra^{\frac{3a-1}{4}} Pr^{\frac{3b}{4}} \Gamma^{3a} \left(\frac{Ra_g}{Ra}\right)^{\frac{3(1+a)}{4}} \Gamma^{-3(1+a)} + \frac{Ra_g}{Ra}\Gamma^{-4} = 1. \tag{A1}$$

Thus,

$$2C_{q_w}^{-3/4} C_{tub}^{3/4} Ra_g^{\frac{3(1+a)}{4}} Pr^{\frac{3b}{4}} \Gamma^{-3} + Ra_g \Gamma^{-4} = Ra. \tag{A2}$$

In terms of Grashof number $Gr = Ra/Pr$, this equation becomes

$$2C_{q_w}^{-3/4} C_{tub}^{3/4} Gr_g^{\frac{3(1+a)}{4}} Pr^{\frac{3(a+b)-1}{4}} \Gamma^{-3} + Gr_g \Gamma^{-4} = Gr. \tag{A3}$$

For the two regimes, we have

$$2C_{q_w}^{-3/4} C_{0.3}^{3/4} Gr_g^{39/40} Pr^{1/2} \Gamma^{-3} + Gr_g \Gamma^{-4} = Gr \quad \text{for} \quad Gr_{g0} < Gr_g < Gr_{gc}, \tag{A4a}$$

$$2C_{q_w}^{-3/4} C_{0.5}^{3/4} Gr_g^{9/8} Pr^{1/2} \Gamma^{-3} + Gr_g \Gamma^{-4} = Gr \quad \text{for} \quad Gr_g > Gr_{gc}. \tag{A4b}$$

The curves traced out by (A4*a*) and (A4*b*) are plotted in a log–log scale in figure 18 for a sample case of $\Gamma = 0.1$ and $Pr = 1$ with variable $C_{q_w} = 0.1328 + 1.235 Ra_d^{-0.18}$. The blue and red curves correspond to the 0.3 regime and the 0.5 regime, respectively. With increasing Grashof number Gr, the gradient Grashof number Gr_g follows the blue curve for lower values less than the critical limit, and above which it follows the red curve. As can be seen, these two curves naturally intersect at the critical gradient Grashof number $Gr_{gc} = 1.6 \times 10^5$ described by the scaling laws of Pawar & Arakeri (2016), which marks the point of transition from the 0.3 to the 0.5 regime in TC. For the particular set of input parameters (Γ, Pr and C_{q_w}) we have selected, this point corresponds to a critical Grashof number (based on total temperature difference) of $Gr_c = 5.3 \times 10^9$. Thus we have the value for the critical Grashof number Gr_c of transition between the scaling regimes, to replace dependency on the gradient-based Grashof number Gr_{gc} in the generalised *Nu*–*Ra* scaling law (4.9) and in the relation for non-dimensional temperature gradient

$\mathrm{d}\widetilde{T}/\mathrm{d}\tilde{z}$ (4.13) or (4.15). The critical Grashof number Gr_c is a very weak function of C_{q_w} which can be seen from the fact that for a choice of $C_{q_w} = 0.1729$, this equation would have yielded $Gr_c = 5.9 \times 10^9$, and for $C_{q_w} = 0.15$, $Gr_c = 6.4 \times 10^9$, neither of which are shown here.

References

Ahlers, G. 2022 Aspect ratio dependence of heat transfer in a cylindrical Rayleigh–Bénard cell. *Phys. Rev. Lett.* **128** (8), 084501.

Ahlers, G., Grossmann, S. & Lohse, D. 2009 Heat transfer and large scale dynamics in turbulent Rayleigh–Bénard convection. *Rev. Mod. Phys.* **81** (2), 503–537.

Arakeri, J.H. 2012 Convection. In *Handbook of Environmental Fluid Dynamics*, vol. One, pp. 489–503. CRC Press.

Arakeri, J.H., Avila, F.E., Dada, J.M. & Tovar, R.O. 2000 Convection in a long vertical tube due to unstable stratification – a new type of turbulent flow? *Curr. Sci.* **79** (6), 859–866.

Arakeri, J.H., Kumar, N. & Mahapatra, O. 2024 A dimensionless heat transfer coefficient for free convection that is more appropriate than Nusselt number. *Phys. Fluids* **36** (8), 085150.

Bodenschatz, E., He, X., van Gils, D.P. & Ahlers, G. 2015 Aspect-ratio dependence of the transition to the ultimate state of turbulent Rayleigh–Bénard convection. In *Proceedings of the 15th European Turbulence Conference (Delft, The Netherlands 25–28 August)*.

Calzavarini, E., Lohse, D., Toschi, F. & Tripiccione, R. 2005 Rayleigh and Prandtl number scaling in the bulk of Rayleigh–Bénard turbulence. *Phys. Fluids* **17** (5), 1–7.

Castaing, B., Gunaratne, G., Heslot, F., Kadanoff, L., Libchaber, A., Thomae, S., Wu, X.-Z., Zaleski, S. & Zanetti, G. 1989 Scaling of hard thermal turbulence in Rayleigh–Bénard convection. *J. Fluid Mech.* **204**, 1–30.

Chandra, D.S.R. 2000 Turbulent mixed convection. Master's thesis, Indian Institute of Science, Bangalore.

Chavanne, X., Chillà, F., Castaing, B., Hébral, B., Chabaud, B. & Chaussy, J. 1997 Observation of the ultimate regime in Rayleigh–Bénard convection. *Phys. Rev. Lett.* **79** (19), 3648–3651.

Chavanne, X., Chillà, F., Chabaud, B., Castaing, B. & Hébral, B. 2001 Turbulent Rayleigh–Bénard convection in gaseous and liquid He. *Phys. Fluids* **13** (5), 1300–1320.

Chillà, F. & Schumacher, J. 2012 New perspectives in turbulent Rayleigh–Bénard convection. *Eur. Phys. J. E* **35** (7), 58.

Cholemari, M.R. & Arakeri, J.H. 2005 Experiments and a model of turbulent exchange flow in a vertical pipe. *Intl J. Heat Mass Transfer* **48** (21–22), 4467–4473.

Cholemari, M.R. & Arakeri, J.H. 2009 Axially homogeneous, zero mean flow buoyancy-driven turbulence in a vertical pipe. *J. Fluid Mech.* **621**, 69–102.

Chong, K.L., Huang, S.-D., Kaczorowski, M. & Xia, K.-Q. 2015 Condensation of coherent structures in turbulent flows. *Phys. Rev. Lett.* **115** (26), 264503.

Chong, K.L. & Xia, K.-Q. 2016 Exploring the severely confined regime in Rayleigh–Bénard convection. *J. Fluid Mech.* **805**, R4.

Doering, C.R. 2020*a* Absence of evidence for the Ultimate state of turbulent Rayleigh–Bénard convection. *Phys. Rev. Lett.* **124** (22), 229401.

Doering, C.R. 2020*b* Turning up the heat in turbulent thermal convection. *Proc. Natl Acad. Sci. USA* **117** (18), 9671–9673.

Funfschilling, D., Brown, E., Nikolaenko, A. & Ahlers, G. 2005 Heat transport by turbulent Rayleigh–Bénard convection in cylindrical samples with aspect ratio one and larger. *J. Fluid Mech.* **536**, 145–154.

Gibert, M., Pabiou, H., Chillà, F. & Castaing, B. 2006 High-Rayleigh-number convection in a vertical channel. *Phys. Rev. Lett.* **96** (8), 084501.

Gibert, M., Pabiou, H., Tisserand, J.-C., Gertjerenken, B., Castaing, B. & Chillà, F. 2009 Heat convection in a vertical channel: plumes versus turbulent diffusion. *Phys. Fluids* **21** (3), 035109.

Globe, S. & Dropkin, D. 1959 Natural-convection heat transfer in liquids confined by two horizontal plates and heated from below. *J. Heat Transfer* **81** (1), 24–28.

Grossmann, S. & Lohse, D. 2000 Scaling in thermal convection: a unifying theory. *J. Fluid Mech.* **407**, 27–56.

Grossmann, S. & Lohse, D. 2001 Thermal convection for large Prandtl numbers. *Phys. Rev. Lett.* **86** (15), 3316–3319.

Grossmann, S. & Lohse, D. 2002 Prandtl and Rayleigh number dependence of the Reynolds number in turbulent thermal convection. *Phys. Rev. E - Stat. Nonlinear Soft Matt. Phys.* **66** (1), 1–6.

GROSSMANN S. & LOHSE D. 2004 Fluctuations in turbulent Rayleigh–Benard convection: the role of plumes. *Phys. Fluids* **16** (12), 4462–4472.

GUNASEGARANE, G.S. & PUTHENVEETTIL, B.A. 2014 Dynamics of line plumes on horizontal surfaces in turbulent convection. *J. Fluid Mech.* **749**, 37–78.

HARTMANN, R., CHONG, K.L., STEVENS, R.J.A.M., VERZICCO, R. & LOHSE, D. 2021 Heat transport enhancement in confined Rayleigh–Bénard convection feels the shape of the container (a). *Europhys. Lett.* **135** (2), 24004.

HE, X., BODENSCHATZ, E. & AHLERS, G. 2020*a* Aspect ratio dependence of the ultimate-state transition in turbulent thermal convection. *Proc. Natl Acad. Sci.* **117** (48), 30022–30023.

HE, X., FUNFSCHILLING, D., NOBACH, H., BODENSCHATZ, E. & AHLERS, G. 2012 Transition to the ultimate state of turbulent Rayleigh–Bénard convection. *Phys. Rev. Lett.* **108** (2), 024502.

HE, X., FUNFSCHILLING, D., NOBACH, H., BODENSCHATZ, E. & AHLERS, G. He *et al.* 2020*b* reply:. *Phys. Rev. Lett.* **124** (22), 229402.

HOWARD, L.N. 1966 Convection at high Rayleigh number. In *Applied Mechanics* (ed. H., GÖRTLER), pp. 1109–1115. Springer.

HUANG, S.-D., KACZOROWSKI, M., NI, R. & XIA, K.-Q. 2013 Confinement-induced heat-transport enhancement in turbulent thermal convection. *Phys. Rev. Lett.* **111** (10), 104501.

IYER, K.P., SCHEEL, J.D., SCHUMACHER, J. & SREENIVASAN, K.R. 2020*a* Classical 1/3 scaling of convection holds up to $Ra = 10^{15}$. *Proc. Natl Acad. Sci. USA* **117** (14), 7594–7598.

IYER, K.P., SCHEEL, J.D., SCHUMACHER, JÖRG, SREENIVASAN, K.R. 2020*b* Reply to, He, *et al,* : the dependence of heat transport law on aspect ratio is still unclear. *Proc. Natl Acad. Sci. USA* **117** (48), 30024–30024.

KRAICHNAN R.H. 1962 Turbulent thermal convection at arbitrary Prandtl number. *Phys. Fluids* **5** (11), 1374–1389.

LINDBORG, E. 2023 Scaling in Rayleigh–Bénard convection. *J. Fluid Mech.* **956**, A34.

LLOYD, J.R. & MORAN, W.R. 1974 Natural convection adjacent to horizontal surface of various planforms. *J. Heat Transfer* **96** (4), 443–447.

LOHSE, D. & SHISHKINA, O. 2024 Ultimate Rayleigh–Bénard turbulence,*Rev. Mod. Phys.* **96**, (3), 035001.

LOHSE, D. & TOSCHI, F. 2003 Ultimate state of thermal convection. *Phys. Rev. Lett.* **90** (3), 0212013.

MALKUS, W.V.R. 1954 The heat transport and spectrum of thermal turbulence. *Proc. R. Soc. Lond. A. Math. Phys. Sci.* **225**, 196–212.

NIEMELA, J.J., SKRBEK, L., SREENIVASAN, K.R. & DONNELLY, R.J. 2000 Turbulent convection at very high Rayleigh numbers. *Nature* **404** (6780), 837–840.

NIEMELA, J.J. & SREENIVASAN, K.R. 2003 Confined turbulent convection. *J. Fluid Mech.* **481** (481), 355–384.

NIEMELA, J.J. & SREENIVASAN, K.R. 2006*a* The use of cryogenic helium for classical turbulence: promises and hurdles. *J. Low Temp. Phys.* **143** (5-6), 163–212.

NIEMELA, J.J. & SREENIVASAN, K.R. 2006*b* Turbulent convection at high Rayleigh numbers and aspect ratio 4. *J. Fluid Mech.* **557**, 411–422.

PANDEY, A., KRASNOV, D., SCHUMACHER, J., SAMTANEY, R. & SREENIVASAN, K.R. 2022 Similarities between characteristics of convective turbulence in confined and extended domains. *Physica D: Nonlinear Phenom.* **442**, 133537.

PANDEY, A. & SREENIVASAN, K.R. 2021 Convective heat transport in slender cells is close to that in wider cells at high Rayleigh and Prandtl numbers. *Europhys. Lett.* **135** (2), 24001.

PAWAR, S.S. 2015 Axially homogeneous turbulent convection at high Rayleigh numbers: scaling laws for flux and spectra. *PhD thesis*, Indian Institute of Science, Bangalore.

PAWAR, S.S. & ARAKERI, J.H. 2016 Two regimes of flux scaling in axially homogeneous turbulent convection in vertical tube. *Phys. Rev. Fluids* **1** (4), 042401.

PUTHENVEETTIL, B.A. & ARAKERI, J.H. 2005 Plume structure in high-Rayleigh-number convection. *J. Fluid Mech.* **542** (−1), 217–249.

PUTHENVEETTIL, B.A., GUNASEGARANE, G.S., AGRAWAL, Y.K., SCHMELING, D., BOSBACH, J. & ARAKERI, J.H. 2011 Length of near-wall plumes in turbulent convection. *J. Fluid Mech.* **685**, 335–364.

ROCHE, P.-E. 2020 The ultimate state of convection: a unifying picture of very high Rayleigh numbers experiments. *New J. Phys.* **22** (7), 073056.

ROCHE, P.-E., CASTAING, B., CHABAUD, B., HÉBRAL, B. & SOMMERIA, J. 2001 Side wall effects in Rayleigh–Bénard experiments. *Eur. Phys. J. B* **24** (3), 405–408.

ROCHE, P.E., GAUTHIER, F., KAISER, R. & SALORT, J. 2010 On the triggering of the ultimate regime of convection. *New J. Phys.* **12** (8), 085014.

SAMUEL R., SAMTANEY R. & VERMA M.K. 2022 Large-eddy simulation of Rayleigh–Bénard convection at extreme Rayleigh numbers. *Phys. Fluids* **34** (7), 2204–03697.

SAMUEL, R.J., BODE, M., SCHEEL, J.D., SREENIVASAN, K.R. & SCHUMACHER, J. 2024 No sustained mean velocity in the boundary region of plane thermal convection. *J. Fluid Mech.* **996**, A49.

SCHEEL, J.D., KIM, E. & WHITE, K.R. 2012 Thermal and viscous boundary layers in turbulent Rayleigh–Bénard convection. *J. Fluid Mech.* **711**, 281–305.

SCHEEL, J.D. & SCHUMACHER, J. 2014 Local boundary layer scales in turbulent Rayleigh–Bénard convection. *J. Fluid Mech.* **758**, 344–373.

SCHEEL, J.D. & SCHUMACHER, J. 2017 Predicting transition ranges to fully turbulent viscous boundary layers in low Prandtl number convection flows. *Phys. Rev. Fluids* **2** (12), 123501.

SCHMIDT, L.E., CALZAVARINI, E., LOHSE, D., TOSCHI, F. & VERZICCO, R. 2012 Axially homogeneous Rayleigh–Bénard convection in a cylindrical cell. *J. Fluid Mech.* **691**, 52–68, 2012.

SHISHKINA, O. 2021 Rayleigh–Bénard convection: the container shape matters. *Phys. Rev. Fluids* **6** (9), 090502.

SHRAIMAN, B.I. & SIGGIA, E.D. 1990 Heat transport in high-Rayleigh–number convection. *Phys. Rev. A* **42** (6), 3650–3653.

SIGGIA, E.D. 1994 High Rayleigh number convection. *Annu. Rev. Fluid Mech.* **26** (1), 137–168.

SKRBEK, L. & URBAN, P. 2015 Has the ultimate state of turbulent thermal convection been observed? *J. Fluid Mech.* **785**, 270–282.

SREENIVASAN K.R. & NIEMELA J.J. 2023 Turbulent convection at very high Rayleigh numbers and the weakly nonlinear theory. *Atmosphere* **14** (5), 826.

STEVENS, R.J.A.M., VAN DER POEL, E.P., GROSSMANN, S. & LOHSE, D. 2013 The unifying theory of scaling in thermal convection: the updated prefactors. *J. Fluid Mech.* **730**, 295–308.

SUN, C., CHEUNG, Y.H. & XIA, K.Q. 2008 Experimental studies of the viscous boundary layer properties in turbulent Rayleigh–Bénard convection. *J. Fluid Mech.* **605**, 79–113.

SUN, C., REN, L.-Y., SONG, H. & XIA, K.-Q. 2005 Heat transport by turbulent Rayleigh–Bénard convection in 1 m diameter cylindrical cells of widely varying aspect ratio. *J. Fluid Mech.* **542**, 165–174.

THEERTHAN, S.A. & ARAKERI, J.H. 1998 A model for near-wall dynamics in turbulent Rayleigh–Bénard convection. *J. Fluid Mech.* **373**, 221–254.

THEERTHAN S.A. & ARAKERI J.H. 2000 Planform structure and heat transfer in turbulent free convection over horizontal surfaces. *Phys. Fluids* **12** (4), 884–894.

TISSERAND, J.-C., CREYSSELS, M., GIBERT, M., CASTAING, B. & CHILLÀ, F. 2010 Convection in a vertical channel. *New J. Phys.* **12** (7), 075024.

URBAN, P., MUSILOVÁ, V. & SKRBEK, L. 2011 Efficiency of heat transfer in turbulent Rayleigh–Bénard convection. *Phys. Rev. Lett.* **107** (1), 014302.

VERZICCO, R. 2002 Sidewall finite-conductivity effects in confined turbulent thermal convection. *J. Fluid Mech.* **473**, 201–210.

VERZICCO, R. & CAMUSSI, R. 1999 Prandtl number effects in convective turbulence. *J. Fluid Mech.* **383**, 55–73.

WU, X.-Z. & LIBCHABER, A. 1992 Scaling relations in thermal turbulence: the aspect-ratio dependence. *Phys. Rev. A* **45** (2), 842–845.

ZHANG, L. 2019 Scalar transport in buoyancy-driven flows and kinematic behavior of magnetotactic bacteria. *PhD thesis*, The Chinese University of Hong Kong, June, Hong Kong.

ZHANG, L. & XIA, K.-Q. 2023*a* Achieving heat transfer enhancement via manipulation of bulk flow structures in turbulent thermal convection. *Phys. Rev. Fluids* **8** (2), 023501.

ZHANG, L., XIA, K.-Q. 2023*b* Heat transfer in a quasi-one-dimensional Rayleigh–Bénard convection cell. *J. Fluid Mech.* **973**, R5.

ZWIRNER, L. & SHISHKINA, O. 2018 Confined inclined thermal convection in low-Prandtl-number fluids. *J. Fluid Mech.* **850**, 984–1008.